JGR Oceans

RESEARCH ARTICLE
10.1029/2021JC017428

Frontal Dynamics in the Alboran Sea: 2. Processes for Vertical Velocities Development

Maximo Garcia-Jove[1], Baptiste Mourre[1], Nikolaos D. Zarokanellos[1], Pierre F. J. Lermusiaux[2], Daniel L. Rudnick[3], and Joaquín Tintoré[1,4]

[1]Balearic Islands Coastal Observing and Forecasting System (SOCIB), Palma de Mallorca, Spain, [2]Department of Mechanical Engineering, Massachusetts Institute of Technology, Cambridge, MA, USA, [3]Scripps Institution of Oceanography, University of California, San Diego, La Jolla, CA, USA, [4]Instituto Mediterráneo de Estudios Avanzados (IMEDEA (CSIC-UIB)), Esporles, Spain

This article is a companion to Zarokanellos et al. (2022), https://doi.org/10.1029/2021JC017405.

Key Points:

- The frontal dynamics was investigated using multi-platform observations and a high-resolution realistic simulation in spring 2018
- The western front vertical velocities were intensified by frontogenesis, instabilities, and Ekman effects
- The eastern front intensification was governed by filamentogenesis associated with a cold filament

Correspondence to:

M. Garcia-Jove,
mgarciajove@socib.es

Citation:

Garcia-Jove, M., Mourre, B., Zarokanellos, N. D., Lermusiaux, P. F. J., Rudnick, D. L., & Tintoré, J. (2022). Frontal dynamics in the Alboran Sea: 2. Processes for vertical velocities development. *Journal of Geophysical Research: Oceans*, *127*, e2021JC017428. https://doi.org/10.1029/2021JC017428

Received 31 MAR 2021
Accepted 13 FEB 2022

Author Contributions:

Data curation: Nikolaos D. Zarokanellos, Daniel L. Rudnick
Formal analysis: Maximo Garcia-Jove, Baptiste Mourre, Nikolaos D. Zarokanellos
Funding acquisition: Joaquín Tintoré
Project Administration: Joaquín Tintoré
Resources: Baptiste Mourre, Nikolaos D. Zarokanellos, Daniel L. Rudnick, Joaquín Tintoré
Software: Maximo Garcia-Jove
Supervision: Baptiste Mourre
Visualization: Maximo Garcia-Jove

Abstract Significant lateral density gradients occur throughout the year in the Alboran Sea, giving rise to two main fronts: the Western Alboran Gyre Front (WAGF) and Eastern Alboran Gyre Front (EAGF), where large vertical velocities often develop. To improve the understanding of the processes that underlie the development of the vertical velocities in the fronts, the periods of development were analyzed in the perspective of the frontogenesis, instabilities, non-linear Ekman, and filamentogenesis mechanisms, using multi-platform in-situ observations and a high-resolution realistic simulation in spring 2018. The spatio-temporal characteristics of the WAGF indicate a wider, deeper, and longer-lasting front than the EAGF. Additionally, the WAGF shows stronger and deeper upwelling and downwelling regions. The WAGF vertical velocities (up to |55| m/day) are amplified by an across-front ageostrophic secondary circulation generated by: (a) frontal intensification explained by frontogenesis, which shows a sharpening of buoyancy gradients associated with the Atlantic Jet, (b) nonlinear Ekman effects, that are enhanced by the persistent western wind blowing along the frontal direction, and (c) submesoscale instabilities (symmetric and ageostrophic baroclinic instabilities). The EAGF vertical velocities (up to |38| m/day) are amplified by two asymmetrical ageostrophic cells developed across the front with a narrow upwelling region in the middle. The cell's circulation is explained by frontal intensification produced by filamentogenesis through a cold filament advection to the Mediterranean Sea interior, that is characterized by pointy isopycnals at the center of the filament. This mechanism is observed in both the model and glider observations.

Plain Language Summary The processes responsible for vertical velocities development at the main fronts of the Alboran Sea were analyzed combining a high-resolution realistic simulation and glider observations in spring 2018. The two fronts were found to be governed by different spatio-temporal dynamics. In the Western Alboran Gyre Front, the vertical velocities are amplified by an across-front ageostrophic circulation generated by the intensification of the front, which is the result of an increase of horizontal density gradients, and along down-front winds. In turn, submesoscale instabilities processes strengthen the vertical velocities in the frontal region, but weaken the front. On the contrary, in the Eastern Alboran Gyre Front, the vertical velocities development is associated with an across-front complex pattern described by two asymmetric ageostrophic motions produced by the frontal intensification, which are the consequence of a cold filament advected in the interior of the Mediterranean Sea. As a result, pointy isopycnals are observed in the front.

1. Introduction

Vertical velocities associated with meso- and submeso-scale structures (Mahadevan, 2016; McWilliams, 2016) generate important vertical fluxes of carbon and other biogeochemical tracers from the surface layer to depths below the mixed layer (Oguz et al., 2017; Ruiz et al., 2019). Vertical velocities are commonly very weak and characterized by small scales which make them difficult to measure. The Alboran Sea in the Western Mediterranean Basin is a highly dynamic system (Renault et al., 2012). The Western and Eastern Alboran Gyre fronts (WAGF and EAGF) are characterized by strong density gradients produced by the encountering of relatively cold and light waters from the Atlantic Ocean with warmer and saltier waters of the Mediterranean Basin. These gradients are generated by the interaction of eddies, meanders, fronts, and filaments and lead to large vertical velocities. The Atlantic Jet (AJ) influences the formation of two large anticyclonic gyres in the western and eastern Alboran Sea (Oguz et al., 2016; Renault et al., 2012). The meso- and submeso-scale structures generated in the Western

Writing – original draft: Maximo Garcia-Jove
Writing – review & editing: Maximo Garcia-Jove, Baptiste Mourre, Nikolaos D. Zarokanellos, Pierre F. J. Lermusiaux, Daniel L. Rudnick, Joaquín Tintoré

Mediterranean Basin are visible for instance in images of ocean color (Figure 1a) and sea surface temperature (SST; Figure 1b). The ocean color imagery presents a large eddy where the larger concentrations of chlorophyll located on its outer part are associated with the WAGF. On the other hand, the SST image shows a penetrating and elongated meander associated with the EAGF that introduces cold water to the interior of the Mediterranean Sea.

The scales of interest in this study are 1–100 km in the horizontal, 0–1,000 m in the vertical, and from a day to several weeks in time. While the large spatio-temporal scales are dominated by the effects of Earth's rotation, which constrain the motion to be largely horizontal to satisfy the geostrophic and the thermal wind balance, the ageostrophic motion and vertical velocities become more important at the smallest scales leading to a non-rotational and unbalanced flow. These ocean scales include mesoscale flows (10–100 km, and a few weeks) characterized by a small Rossby number, $Ro \ll 1$, and a large Richardson number, $Ri = N^2/U_z$ (where N^2 is the buoyancy frequency and U_z is the vertical gradient of the horizontal velocity). At smaller scale, the submesoscale flows (1–10 km, and a few days) occur with $\mathcal{O}(1)$ Ro and Ri. These processes are driven by internal instabilities, buoyancy forcing or wind stress at the surface (Mahadevan, 2016; McWilliams, 2016). At the mesoscale, the flow is predominantly two-dimensional as the magnitude of the vertical velocities (W) is several orders of magnitude smaller than the horizontal velocities, $w \approx \mathcal{O}$(1–10 m/day). Nevertheless, the magnitude of the vertical velocities increases as a smaller spatio-temporal scale is approached. For submesoscale $W \approx \mathcal{O}$(100 m/day) as a result of ageostrophic motions (Mahadevan, 2016).

Important efforts have historically been made to measure vertical velocities in the frontal zones of the Alboran Sea (Pascual et al., 2017; Tintoré et al., 1991; Vélez-Belchí & Tintoré, 2001). For example, in the Western Alboran Sea, Tintoré et al. (1991) used a quasi-geostrophic omega equation to estimate vertical velocities around 20–30 m/day related to the mesoscale circulation. In the Eastern Alboran Sea, Ruiz et al. (2019) found vertical velocities of 10 m/day associated with a large-scale circulation. The vertical velocities from the quasi-geostrophic omega equation is valid for the mesoscale flow. However, this equation fails to capture $\mathcal{O}(1)$ Rossby number dynamics associated with submesoscales. For these small scales better approximations should include the advection of ageostrophic velocities terms (Mahadevan, 2016).

The circulation of the flow at the front is defined primarily by an along-front jet and an across-front ageostrophic secondary circulation (ASC; McWilliams, 2016). The jet separates dense waters with positive relative vertical vorticity (ξ) and light waters with negative ξ; meanwhile, the ASC is characterized by upward velocities in the front's light side and downward velocities in the dense side. The project entitled Coherent Lagrangian Pathways from the Surface Ocean to Interior (CALYPSO, Office of Naval Research initiative (Mahadevan et al., 2021)) addresses the challenges of observing, understanding, and predicting the vertical velocities and three dimensional pathways on subduction processes of the fronts in the Alboran Sea. Within this scope, the focus of this paper is

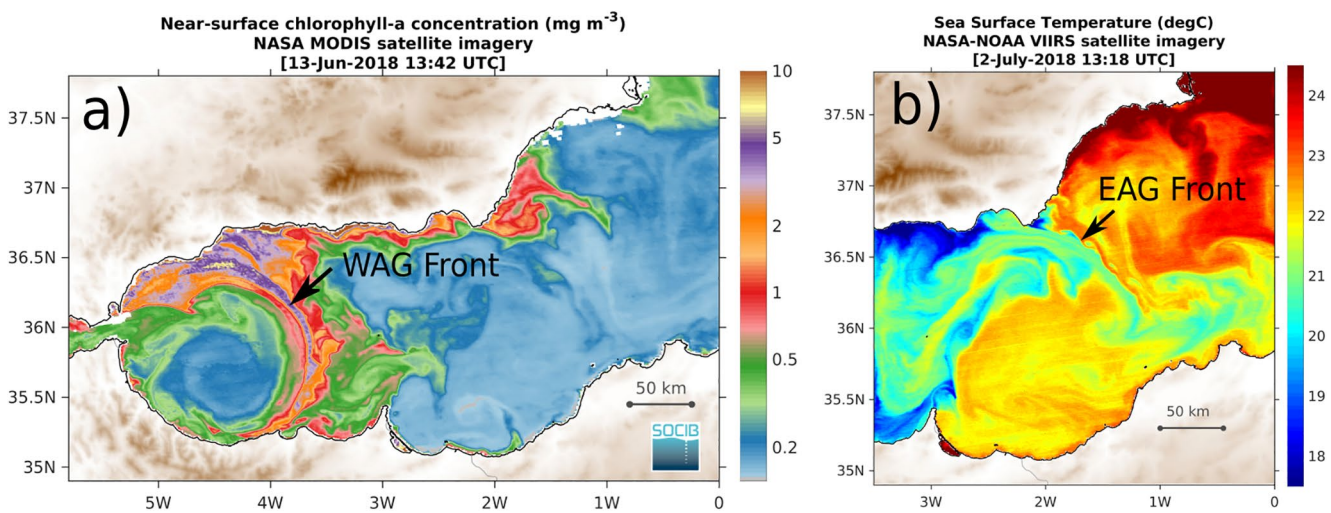

Figure 1. Satellite images of the Alboran Sea: (a) chlorophyll concentration (mg m^{-3}) from MODIS satellite on 13 June 2018 showing the intensification of the Western Alboran Gyre Front and (b) mesoscale cold meander intrusion observed in sea surface temperature (°C) from VIIRS/NPP on 2 July 2018 corresponding to the intensification of the Eastern Alboran Gyre Front.

to understand the processes that underlie the frontal intensification and the development of the vertical velocities in the WAGF and EAGF using high spatio-temporal observations and a high-resolution numerical model simulation. For this paper, the observational component of the CALYPSO project included an Underway-Conductivity-Temperature-Depth (UCTD) measurements (Dever et al., 2019; Rudnick & Klinke, 2007) during the research cruise in the Alboran Sea in May-June 2018, and high spatio-temporal hydrographic and velocity measurements from multiple glider transects across three parallel segments crossing the EAGF.

The specific aims of the present research are to (a) evaluate the development of vertical velocities in the WAG and EAG fronts with a realistic numerical model, validated by high-resolution in-situ observations; (b) analyze the driving mechanisms of frontal intensification in both fronts. The paper is organized as follows: a review of the frontal intensification mechanisms and vertical velocities development processes is provided in Section 2. The CALYPSO 2018 observations and numerical simulation of the Alboran Sea setup are presented and compared in Section 3. General results are described in Section 4, where the differences in the vertical velocities development observed at the WAG and EAG fronts are presented. Additionally, in this section we review and analyze the mechanism responsible for frontal intensification and vertical velocities development. Finally, we discuss the relevance of each mechanism and its contribution to the WAG and EAG fronts in Section 5. A companion paper (Zarokanellos et al., 2022) specifically analyses glider observations during the same period to identify the 3D coherent pathways from the surface to the ocean interior in the EAGF.

2. Background on Vertical Velocities Development Processes at Frontal Regions

The vertical velocities development can be produced by frontal intensification, instabilities processes, nonlinear Ekman effects, and filamentogenesis. A brief description of each process is described below.

1. Strain-induced frontogenesis mechanism: Mahadevan and Tandon (2006) and Mahadevan (2016) suggest that frontal intensification is produced by a horizontal density gradient intensification in the presence of a large lateral strain rate and convergence in the flow (Hoskins & Bretherton, 1972). As a result, the relative vertical vorticity (ξ) equals or exceeds the planetary vorticity f, where ξ is produced by large shear velocities and sharp buoyancy gradients in the cross-frontal direction. The intensification of ξ favors the collapsing of the geostrophic balance in the along-front direction. Consequently, the local vorticity-based Rossby number $Ro = |\xi|/f$ becomes $\mathcal{O}(1)$, and the loss of geostrophic balance leads to a single ASC (across the front), which acts to restore the geostrophic and thermal wind balance at the front. Finally, the vertical velocities are increased by the contribution of the ASC. In the case of WAGF, Oguz et al. (2016, 2017) using numerical simulations pointed out that phytoplankton production was modulated by the frontogenesis mechanism and intensified by the ASC. Meanwhile, based on glider measurements in the EAGF region, Ruiz et al. (2019), proposed that frontal intensification was produced by frontogenesis, which enhances the relative vertical vorticity leading to large local Rossby numbers resulting in the generation of an ASC responsible for large vertical excursions of biochemical tracers in the front. More recently, Capó et al. (2021) analyzed the intermittent character of frontogenesis in the Alboran Sea using a high-resolution simulation over a 3-year period.
2. Instabilities processes: the symmetric (Bachman et al., 2017), gravitational (Haine & Marshall, 1998), ageostrophic baroclinic instability (Boccaletti et al., 2007), and ageostrophic anticyclonic baroclinic instability (McWilliams et al., 2004) can lead to vertical velocities development together with a weakening of the frontal gradients. The wind tends to reduce the Ertel potential vorticity (EPV) and modifies the stratification in the upper ocean, making the fronts susceptible to symmetric instability (SI) and gravitational instability. SI is an overturning instability that arises in baroclinic flows featuring a lateral density gradient and an associated vertically sheared geostrophic flow (Bachman et al., 2017). SI removes kinetic energy from the flow (Thomas et al., 2016). Gravitational instability is associated with denser and deeper fluid overlying lighter fluid through upright convection (Haine & Marshall, 1998). Within the surface mixing layer, the ageostrophic instabilities are developed at the frontal density gradients enhancing upper ocean restratification (Fox-Kemper et al., 2008). Finally, ageostrophic anticyclonic baroclinic instability is developed along the front within the mixed layer, it can arise by the loss of balance in submesoscale features (Molemaker et al., 2005). In the Alboran Sea, instabilities processes have been related to vertical exchange in the frontal regions. In the WAGF region, the emerging of more pronounced instability features are associated with the intensification of the AJ (Oguz et al., 2016; Robinson et al., 1999). Meanwhile, based on numerical simulations in the EAGF region, Ruiz et al. (2019) suggested that the presence of SI did not extend below 40 m depth. Therefore, subduction

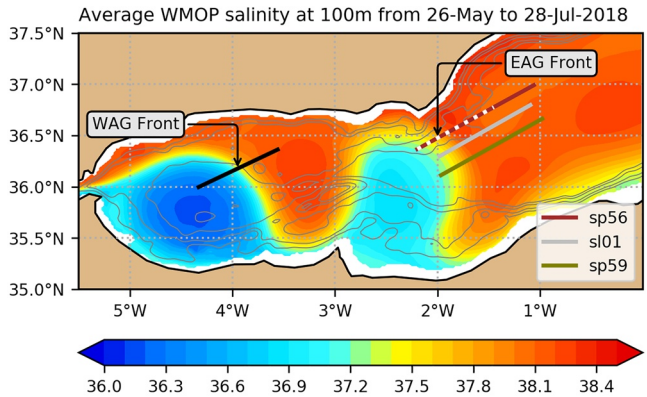

Figure 2. Temporal mean over the study period of the Western Mediterranean OPerational system simulated salinity field, at 100 m depth in the Alboran Sea. The black line and white dotted line indicate the Western Alboran Gyre Front and Eastern Alboran Gyre Front cross section, respectively, used in this study. The color lines indicate the glider trajectories from sp56 (red), sl01 (gray), and sp59 (green), platforms which cross the EAG front.

of Chl observed down to 100 m was interpreted to occur in response to baroclinic instability. At an initial stage, baroclinic instabilities can be developed on the border of the front due to the release of available potential energy from the density gradient intensification and reinforce the ASC, leading to frontal intensification due to horizontal velocity and buoyancy gradients. However, at a subsequent stage these instabilities have a frontolytic effect which stops the frontogenesis process (Sullivan & McWilliams, 2018).

3. Nonlinear Ekman effects: along down-front winds lead to frontogenesis. Thomas and Lee (2005) indicated that along front wind generates downwelling produced by an across-front Ekman transport at the surface. As a result, the transport generated drives dense water over the light side producing an ASC cell. Additionally, the along front winds are related to frictional forces that extract EPV at the surface frontal outcrop (Thomas, 2005). Furthermore, the wind stress generates Ekman currents which destratify (down-front winds) and restratify (up-front winds) the mixed layer. Finally, the nonlinear Ekman transport in addition to the ASC intensification can increase vertical velocities. In the WAGF region, Oguz et al. (2017) proposed that the westerly (down-front) winds in the direction of the AJ improved the frontogenetic plankton production by intensifying the ASC. Additionally, the down-front winds are associated with the southward nonlinear Ekman transport from the northern coast, which induces an increase in surface water density on the dense side of the jet and introduces a convective mixing near the surface.
4. Filamentogenesis mechanism: this is a particular case of frontogenesis, in which a cold filament leads to frontal intensification. In theoretical and experimental cases, McWilliams et al. (2009) and Gula et al. (2014) shown that surface buoyancy gradients and ASC are intensified by strain flow as a result of an elongated and cold submesoscale filament structure. Consequently, the vertical velocities are intensified by two ASC cells on both sides of the filament and a sharp upwelling at the center of the filament. Observations (von Appen et al., 2018) and realistic simulations (Dauhajre et al., 2017; Gula et al., 2014) have been used to diagnose and describe filament circulation in different regions.

3. Observations and Numerical Simulation of the Alboran Sea

Coherent gyres and fronts in the Alboran Sea were studied with high spatio-temporal resolution using the multi-platform system of CALYPSO field campaign in 2018 and a high-resolution realistic simulation of the Western Mediterranean Sea. The CALYPSO 2018 experiment and Alboran Sea simulation configuration are described in this section. Additionally, the characteristics of the Alboran Sea circulation in the simulation are compared to available in-situ observations.

3.1. CALYPSO Observation Program Description

The CALYPSO 2018 field campaign took place from 27 May to 2 June 2018, using two research vessels (NRV Alliance and NRV SOCIB), with the objectives of (a) identifying subduction regions in the Alboran Gyres and (b) measuring vertical velocities by tracking physical, chemical, and biological tracers. Shipboard UCTD casts (Dever et al., 2019) were conducted across the WAG and collected temperature, conductivity, and pressure measurements (Figure 3a). Additionally, three gliders (two Sprays sp56 and sp59 (Rudnick, 2021) and one Slocum sl01 (Zarokanellos et al., 2021)) were deployed in the northeastern region of the Alboran Sea (Figure 2). In Figure 3a, the plan view at 100 m depth of the salinity from the UCTD and model average over CALYPSO 2018 campaign shows large meanders and fronts that divide Atlantic and Mediterranean waters. The Mediterranean saltier and warmer waters are located between two Atlantic fresher water sectors. Moreover, the glider measurements in the study provided long-term observations of the EAGF temporal variability with a high spatial resolution by profiling the upper 700 m in a sawtooth pattern of consecutive dive cycles that were completed every ~5 hr over a distance of 3–5 km. The gliders were deployed in three parallel lines taking physical and biogeochemical meas-

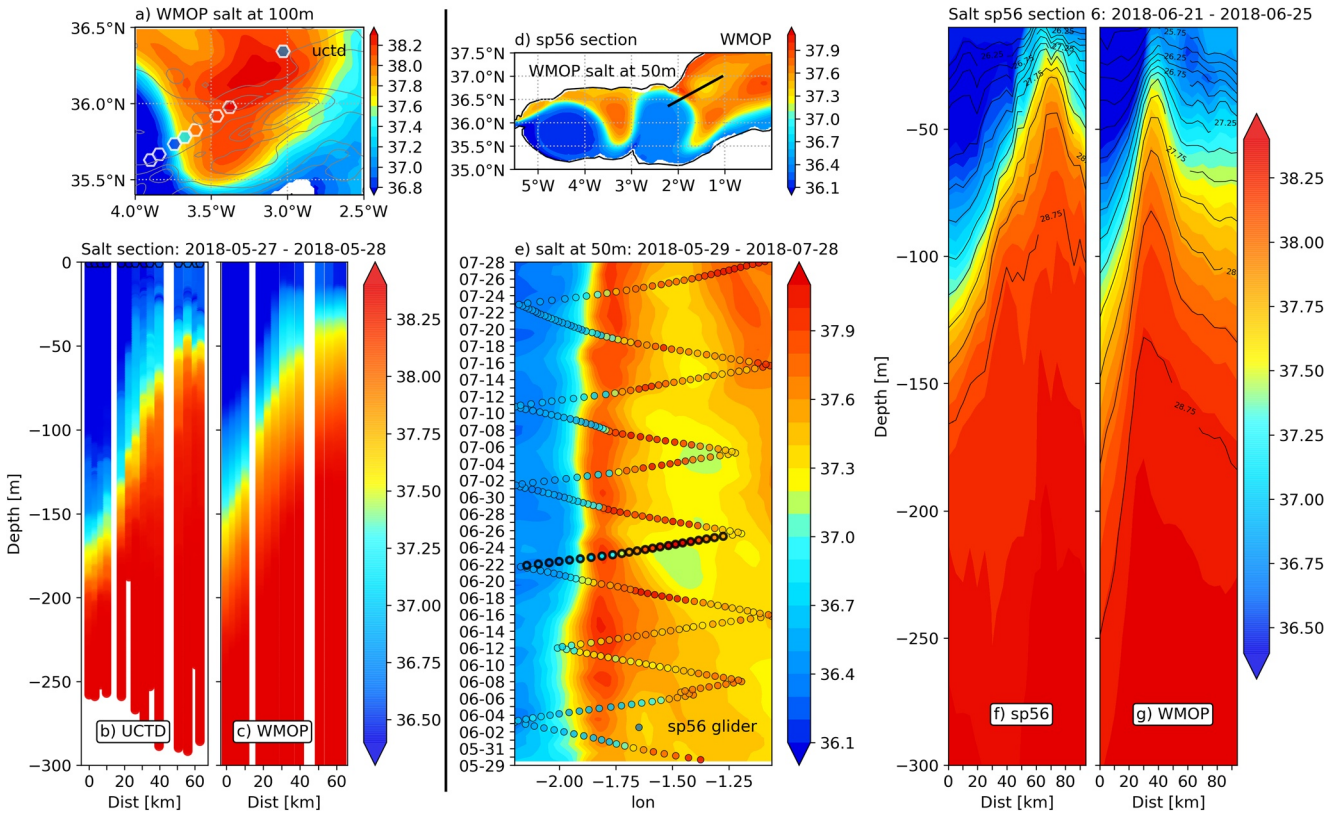

Figure 3. CALYPSO 2018 observation and Western Mediterranean OPerational system (WMOP) daily averaged simulation comparison: (a) Map of salinity from Underway-Conductivity-Temperature-Depth (UCTD) casts (hexagon markers) and temporal mean of WMOP at 100 m depth from 27 May to 28 May. (b and c) Vertical section of the salinity across the Western Alboran Gyre Front (section white hexagonal) from UCTD casts (b) and WMOP (c). (d) Salinity map from the WMOP temporal mean over the glider campaign and sp56 glider path (black line). (e) Hovmöller diagram at 50 m along the sp56 glider path in June to July 2018 from WMOP. The circles indicate the salinity observed from the sp56 glider path during the 12 transects. (f and g) Vertical structure of the salinity in the Eastern Alboran Gyre Front from sp56 glider and WMOP.

urements for 72 days and collecting over 34 across-front sections between 24 May to 3 August 2018. The glider sensors platforms, and data processing are described in detail in Zarokanellos et al. (2022).

3.2. Simulation of the Alboran Sea

3.2.1. Model Setup

A high-resolution simulation from the Western Mediterranean OPerational system (WMOP; Juza et al. (2016); Mourre et al. (2018)), developed at the Balearic Islands Coastal Observing and Forecasting System (Tintoré et al., 2013) was used in this study. WMOP uses a regional configuration of the Regional Ocean Modeling System (ROMS; Shchepetkin & McWilliams, 2005), covering the Western Mediterranean Sea, from the Strait of Gibraltar to the Sardinia Channel. The vertical grid is made of 32 stretched sigma levels (resulting in a vertical resolution varying from 1 to 2 m at the surface, 30–40 m at 200 m depth, around 250 m at 1,000 m depth, and 500 m for depth levels deeper than 2,500 m). The horizontal grid comprises 631 × 539 points with a resolution varying from 1.8 to 2.2 km. The bathymetry is derived from the 1 arc-minutes grid resolution topography database of Smith and Sandwell (1997). The model is forced at the surface by the hourly and 5 km spatial resolution HIRLAM atmospheric model provided by the Spanish National Meteorological Agency (AEMET). WMOP forecasts product use initial state and boundary conditions from the coarser grid Mediterranean model of the Copernicus Marine Environment Monitoring Service (CMEMS). WMOP includes data-assimilation obtained with an Ensemble Optimal Interpolation method (Hernandez-Lasheras & Mourre, 2018) with 3 days cycles, assimilating data from satellites (Sea Level Anomalies and SST) and Argo profiles (temperature and salinity).

In this work, a specific free-run WMOP simulation was developed to get a simulation as realistic as possible, but at the same time fully governed by the model dynamics so as to investigate dynamical processes. The free-run simulation was initialized from the outputs of the data-assimilative forecasts (https://socib.es/?seccion=modelling&facility=forecast) on 23 May 2018, but did not include any further data assimilation updates. Note that the simulation used in this study did not assimilate any in-situ CALYPSO 2018 data. The WMOP free-run simulation analyzed in this study was run over a period of 2 months until 31 July 2018. Daily average numerical outputs of the full three-dimensional prognostic variables were used to significantly limit the influence of inertial waves in the analysis of the frontal intensification and vertical velocities development. The 2 km spatial resolution of the WMOP grid provides an advantage to resolve the ageostrophic and submesoscale processes compared to CMEMS models. Moreover, the use of a free-run simulation allows us to analyze ocean dynamics as represented by the model equations. Notice that the Alboran Sea is a subdomain of the whole WMOP domain.

3.2.2. Alboran Gyres and Fronts

The spatial distribution of salinity at 100 m depth (Figure 2) in the simulation shows two main anticyclonic gyres of the Alboran Sea associated with the meandering AJ. These gyres are known as the Western Alboran Gyre and Eastern Alboran Gyre and give rise to two main fronts which we are identified as the WAGF and EAGF. The WAGF and EAGF were observed during the CALYPSO 2018 experiment respectively by UCTD and glider platforms, and reproduced in the WMOP simulation (Figure 3). The vertical sections of the salinity from WMOP simulation (Figures 3c and 3g) are obtained by the interpolation of the model outputs onto the exact times and locations of the UCTD and glider observations. In Figures 3a–3c, the UCTD data and model display similar scales and patterns of enhanced variability in the salinity field. Strong lateral salinity gradients (at 100 m depth, $\Delta_{salt} \sim 1.5$ salinity units over 25 km across WAGF) are observed across the WAGF, with a realistic vertical structure in the model, associated with the WAG.

On the other hand, the sp59, sl01, and sp56 gliders trajectories crossed the EAGF on several occasions. Model validation along the sp56 glider section are shown in Figures 3d–3f and 3g. The cross-front salinity structure obtained from glider observations (Figure 3f) and the model (Figure 3g) shows a good agreement in term of density gradients and isopycnal slopes depicting a bell-shaped pattern. However, the front is shifted to the northeastward by around 30 km in the model. The temporal variability of the EAGF position is illustrated with the Hovmöller diagram calculated along the sp56 glider path (Figure 3c) for both glider and model data. It indicates that glider observations show a frontal displacement of about 30 km in the northeast direction, while the model shows a more fixed frontal position. It confirms the slight spatial shift of the EAGF in the model, consistent with the results of Rypina et al. (2021) based on a comparison with surface drifters. The high spatio-temporal variability observed in the EAGF is discussed in details in Zarokanellos et al. (2022) analyzing observations from the three CALYPSO gliders together with satellite images. We limit here the analysis to the validation of the main characteristic of the front in the model. Overall, the numerical simulation is able to reproduce the ageostrophic and submesoscale processes of both WAG and EAG fronts in terms of gradients and vertical structure, providing an appropriate tool to investigate vertical velocities development.

4. Processes for Vertical Velocities Development in the Alboran Sea

The inflow of Atlantic water though the Strait of Gibraltar gives rise to a zonal jet (AJ), which was present in the Alboran Sea in May 2018. This large mesoscale feature associated with horizontal scales about $\mathcal{O}(100)$ km long, small Rossby number, and large Ri is characterized by meridional changes of $\mathcal{O}(1)$ °C in the SST and $\mathcal{O}(1)$ psu in the sea surface salinity over $\mathcal{O}(50)$ km wide, which are observed in Figures 2 and 3. The confluence of the lighter Atlantic and denser Mediterranean waters generates large lateral buoyancy gradients or density fronts along the AJ, which is propitious to the development of large vertical velocities (Ruiz et al., 2019; Tintoré et al., 1991). This paper is focused on the EAG and WAG frontal regions, as illustrated in Figure 2, where the lateral buoyancy and velocity gradients are higher. The WAGF section is located in the region upstream of the WAG seeking to minimize the impact of the complex Alboran ridge bathymetry. The EAGF section is located along the sp56 glider path in the northwestern part of the EAG. It should be noted that both WAG and EAG frontal regions occur all along the AJ.

In the Alboran Sea simulation, the salinity gradients across the WAGF reached a maximum on 12 June 2018 (figure not shown). This lateral salinity gradient intensification has a temporal scale of about 7 days and a spatial

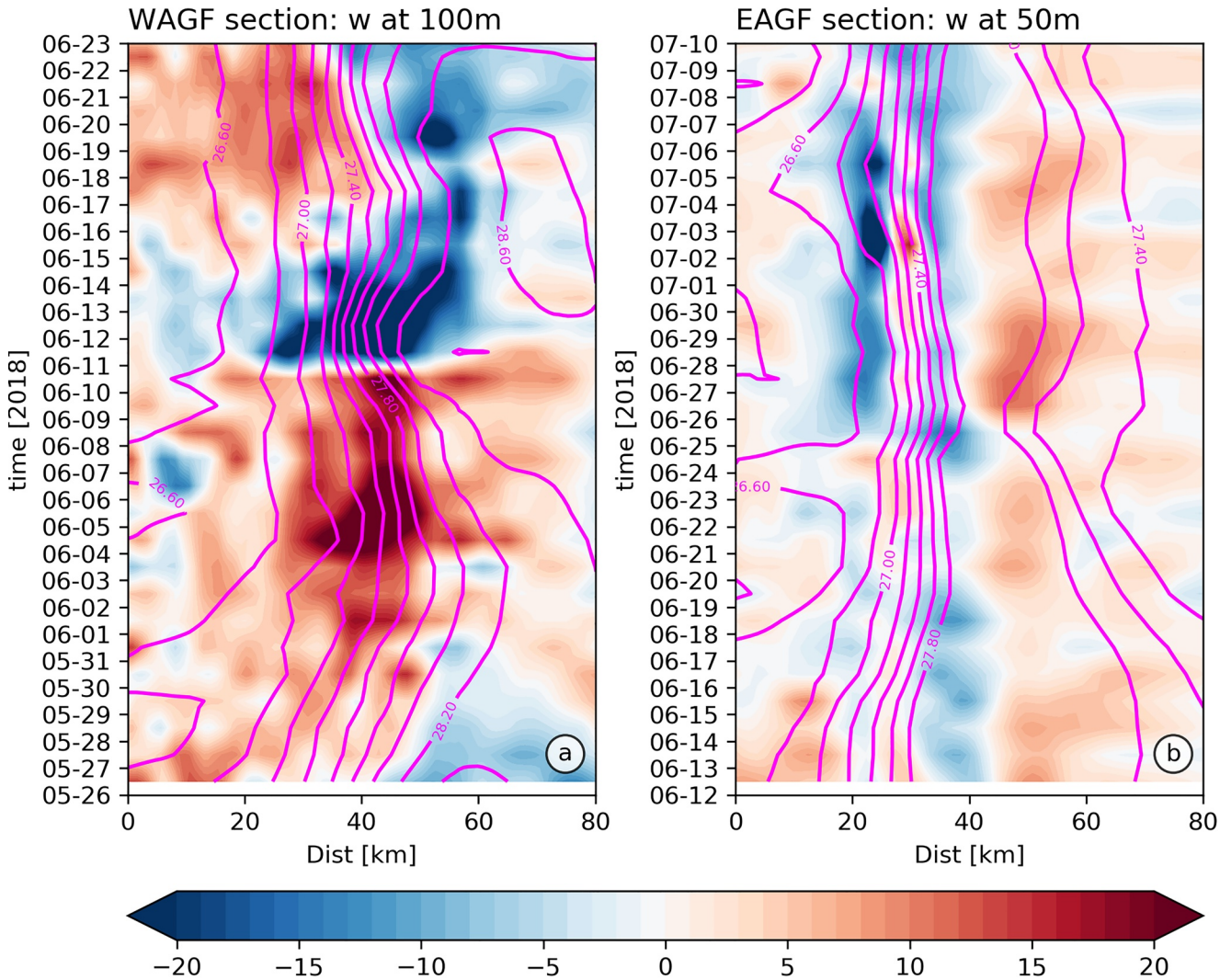

Figure 4. Hovmöller diagram of vertical velocities from Western Mediterranean OPerational system (WMOP) simulation in the (a) Western Alboran Gyre Front (WAGF) and (b) Eastern Alboran Gyre Front (EAGF). For the WAGF, the velocities are plotted at 100 m depth and the period is 26 May to 23 June in 2018. For the EAGF, the velocities are plotted at to 50 m depth and the period is 12 June to 10 July in 2018. The Hovmöller diagrams are calculated from WMOP daily averaged values along the WAGF (black line) and EAGF (white dotted line) sections in Figure 2. The magenta lines represent isopycnals.

scale of about 20–50 km wide across the front. On the other hand, in the model the spatio-temporal variability of the salinity along the EAGF section is lower than that found in the glider observations (see Section 3.2). In the EAGF, the maximum salinity gradients occur on 2 July 2018. The spatio-temporal scales of the gradient intensification in the EAGF in the simulation are about 20–30 km wide and about 4 days. As a comparison, glider observations indicate a 10–45 km cross-frontal scale (Zarokanellos et al., 2022). After describing the spatio-temporal scales characteristics of the WAGF and EAGF, the intensification and processes associated with the vertical velocities are discussed in the next paragraph.

4.1. Vertical Velocities Intensification in the WAGF and EAGF

The spatio-temporal variability of the vertical velocities for the periods where frontal intensification are observed in the WAGF and EAGF sections is presented in Figure 4. The Hovmöller diagrams of the vertical velocities are calculated from WMOP simulation at 100 m depth along the WAGF section and 50 m depth along the EAGF section. These depths correspond to the largest lateral salinity gradient observed in the UCTD (Figure 3b), glider (Figure 3f), and model data (Figures 3c and 3g), respectively for each frontal section. In the WAGF, the vertical

velocities across the front at 100 m depth for the period 26 May to 23 June 2018 (Figure 4a) indicate the generation of two intense and extended up- and down-welling regions. While the upwelling occurs from 4 to 10 in June over 20 km cross-front extension, the downwelling is observed from 11 to 18 in June over a 30 km extension. The WAGF intensification coincides with large downwelling regions on June 12. On the other hand, the development of the vertical velocities at 50 m depth along the EAGF section for the period 12 June to 10 July 2018 is presented in Figure 4b. There is no EAGF upwelling region similar to the WAGF. In contrast to the previous situation, the EAGF section shows an intensification of the downwelling velocities from 2 to 6 July. Additionally, the downwelling region is squeezed into an approximate 10 km extension and is located approximately at 2°W in the EAGF section. The smaller extension and shorter duration of the downwelling region along the EAGF section are consistent with the low spatial-temporal variability observed in the Hovmöller diagram of the salinity (Figure 3e).

The downwelling vertical velocities generated at the EAGF present a different behavior than the vertical velocities observed at the WAGF. These differences in the patterns of the vertical velocities development across the WAGF and EAGF suggest that the processes related to the intensification of the vertical velocities are distinct in the fronts. The following sections examine these processes in detail.

4.2. Frontogenesis Mechanism

Key elements of the generation of the vertical motion are the meso- and submeso-scale dynamics processes in frontal zones (Klein & Lapeyre, 2009; Lapeyre & Klein, 2006; Mahadevan & Tandon, 2006; Sasaki et al., 2014). In the Alboran Sea, mesoscale fronts and meanders were observed (Ruiz et al., 2019; Tintoré et al., 1991; Vélez-Belchí & Tintoré, 2001), identified by large lateral buoyancy and velocity gradients, which are intensified in regions of strain and vorticity that are originated by meandering of the frontal jet due to baroclinic instability (Allen et al., 2001; Mahadevan, 2016).

The presence of lateral strain rate, $S = \left((u_x + v_y)^2 + (v_x + u_y)^2\right)^{1/2}$, and horizontal divergence, $\delta = u_x + v_y$, intensify the horizontal density and velocity gradients producing frontogenesis and hence large vertical velocities (Hoskins, 1982; Hoskins & Bretherton, 1972). The large vorticity is produced in the vicinity of the high strain rate by mesoscale processes. It generates a loss of geostrophic balance along the front flow and an ASC across the section of the front (Capet et al., 2008; McWilliams, 2016). This circulation is described as an overturning cell motion, which restores the geostrophic balance at the front with a vertical motion in the upward direction associated with the surface flow divergence (front's light side) and in a downward direction responsible for a surface flow convergence (front's dense side). The vertical velocities in the downward direction are found to be larger than in the upward direction. Additionally, the vertical motion induces extra vertical vorticity by vertical vortex stretching. On the light side of the front, vortex stretching generates anticyclonic vorticity, and vice versa on the dense side. The surface relative vorticity field develops a stronger cyclonic than anticyclonic vorticity explained by the strain-induced frontogenesis theory (Hoskins, 1982; McWilliams, 2016). Hence, the frontogenesis mechanism develops large negative vertical velocity, which tends to intensify the positive vorticity due to a large amplification factor of $f + \xi$ and resulting in a stronger downwelling on the dense water side located along the frontal region.

On other hand, strain-induced frontogenesis was investigated with the frontal tendency equation. Initially, the intensification of the front was studied through the calculation of the density gradient sharpening evolution (Capet et al., 2008). Later, Gula et al. (2014) used the buoyancy gradient evolution as an indicator of the frontal intensification. More recently, McWilliams et al. (2015) reported that velocity gradient intensification captures more correctly the evolution of the frontogenesis. Pursuing this criteria, the frontal tendency equation refers to the amplitude rate of the change of velocities gradient following a fluid parcel defined as

$$\mathrm{T}^{\mathrm{U}} = \frac{1}{2}\frac{\mathrm{D}|\nabla_{\mathrm{h}}\boldsymbol{U}|^2}{\mathrm{Dt}} = \frac{1}{2}\frac{\mathrm{D}}{\mathrm{Dt}}\begin{pmatrix} |\nabla_{\mathrm{h}}\boldsymbol{u}|^2 \\ |\nabla_{\mathrm{h}}\boldsymbol{v}|^2 \end{pmatrix}, \tag{1}$$

where D/Dt is the material derivative and $\boldsymbol{U} = (\boldsymbol{u}, \boldsymbol{v})$ is the velocities field.

The frontal tendency equation is decomposed into several contributing terms that have been described in McWilliams et al. (2015). At the (sub)-mesoscale, the horizontal advection term in the frontal tendency equation is

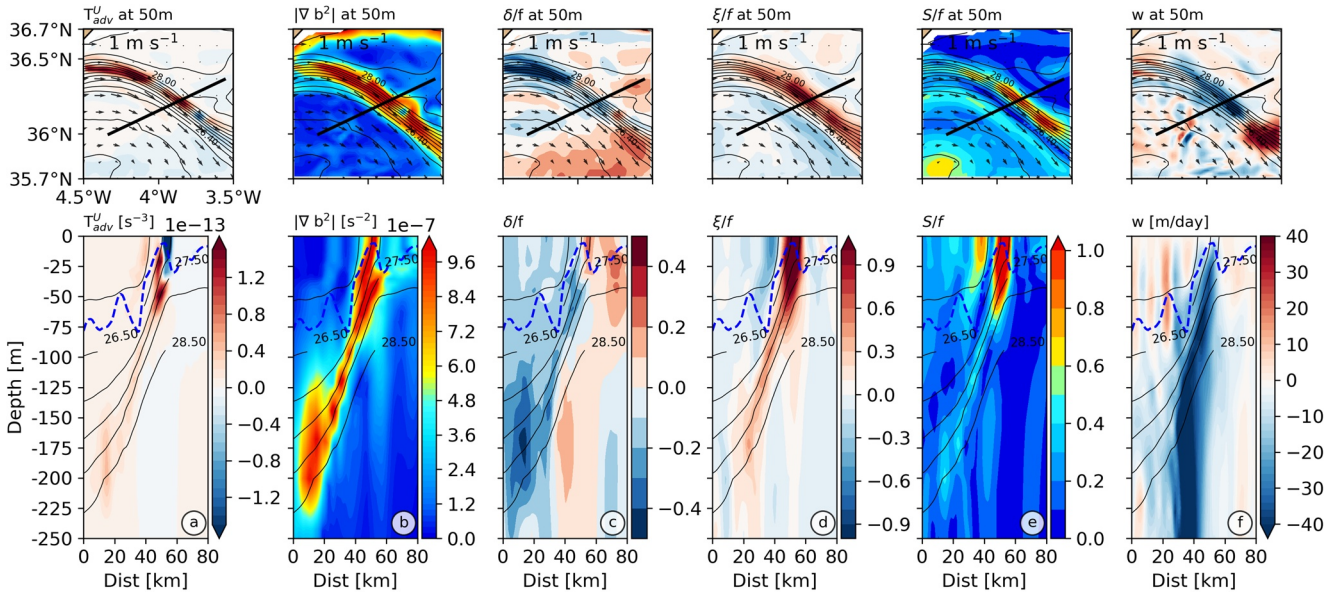

Figure 5. Diagnosis of the frontogenesis mechanism in the Western Alboran Gyre Front on 12 June 2018 from Western Mediterranean OPerational system daily averaged simulation. Map at 50 m depth and vertical structure: (a) advective frontal tendency, (b) lateral buoyancy gradient, (c) horizontal divergence, (d) vertical relative velocity, (e) horizontal strain rate, and (f) vertical velocities. In the maps, the potential density anomaly contours (black lines, contour interval is 0.2 kg m^{-3}) and the section by the black line are also displayed. The black vectors show the 50 m depth currents. In the vertical sections, the solid black lines indicate the position of the isopycnals. The blue dashed line shows the mixed layer depth diagnosed as the depth at which the density exceeds the surface density by 0.05 kg m^{-3}.

predominant in the frontogenesis process (Capet et al., 2008; Dauhajre et al., 2017; Gula et al., 2014). The advective frontal tendency is defined as

$$\mathrm{T}^{\mathrm{U}}_{\mathrm{avd}} = \boldsymbol{Q}^{\boldsymbol{U}}_{\boldsymbol{avd}} \cdot \nabla_{\mathrm{h}} \boldsymbol{U}, \tag{2}$$

where

$$\boldsymbol{Q}^{\boldsymbol{U}}_{\boldsymbol{avd}} = \begin{pmatrix} \boldsymbol{Q}^{\boldsymbol{u}}_{\boldsymbol{avd}} \\ \boldsymbol{Q}^{\boldsymbol{v}}_{\boldsymbol{avd}} \end{pmatrix} = \begin{pmatrix} -u_x \nabla_{\mathrm{h}} \boldsymbol{u} - u_y \nabla_{\mathrm{h}} \boldsymbol{v} \\ -v_x \nabla_{\mathrm{h}} \boldsymbol{u} - v_y \nabla_{\mathrm{h}} \boldsymbol{v} \end{pmatrix}, \tag{3}$$

$\mathrm{T}^{\mathrm{U}}_{\mathrm{avd}}$ is the sum of the advection tendency for u and v gradients $\left(\mathrm{T}^{\mathrm{U}}_{\mathrm{avd}} + \mathrm{T}^{\mathrm{v}}_{\mathrm{avd}} = \boldsymbol{Q}^{\boldsymbol{u}}_{\boldsymbol{avd}} \cdot \nabla_{\mathrm{h}} \boldsymbol{u} + \boldsymbol{Q}^{\boldsymbol{v}}_{\boldsymbol{avd}} \cdot \nabla_{\mathrm{h}} \boldsymbol{v}\right)$. Depending on the sign of the advective frontal tendency term, its contribution amplifies or reduces the velocity gradients; if $\mathrm{T}^{\mathrm{U}}_{\mathrm{avd}} > 0$ the contribution is frontogenetic, while if $\mathrm{T}^{\mathrm{U}}_{\mathrm{avd}} < 0$ the term is frontolytic. In the following subsections, the development of the vertical velocities in the WAGF and EAGF are examined using the Alboran Sea simulation.

4.2.1. WAG Front

The first indicators of the frontogenesis mechanism are identified with the isopycnal magenta lines in the Hovmöller diagram along the WAGF section on 12 June 2018 (Figure 4a). We observe a convergence of isopycnal, increasing the buoyancy horizontal gradients, coincident with the occurrence of the intense downwelling process. The vertical section along the front and plan views at 50 m depth of the principal indicators of the frontogenesis obtained from the WMOP simulation are shown in Figure 5. They correspond to the advective frontal tendency term $\left(\mathrm{T}^{\mathrm{U}}_{\mathrm{avd}}\right)$, lateral buoyancy gradient ($|\nabla b^2|$), divergence (δ/f), vertical relative velocity (ξ/f), horizontal strain rate (S/f), and vertical velocities (w).

In Figure 5, the positive advective frontal tendency in the middle of WAGF section indicates a frontal intensification. Additionally, the lateral buoyancy gradient shows large values along the front corresponding to the confluence of the Atlantic waters with the resident Mediterranean waters. The maps show a high horizontal strain in the frontal region associated with a positive $\mathrm{T}^{\mathrm{U}}_{\mathrm{avd}}$ that enhances the lateral buoyancy gradients and the flow convergence in the region. The vertical structure of the WAGF shows an intense front extending to 180 m depth

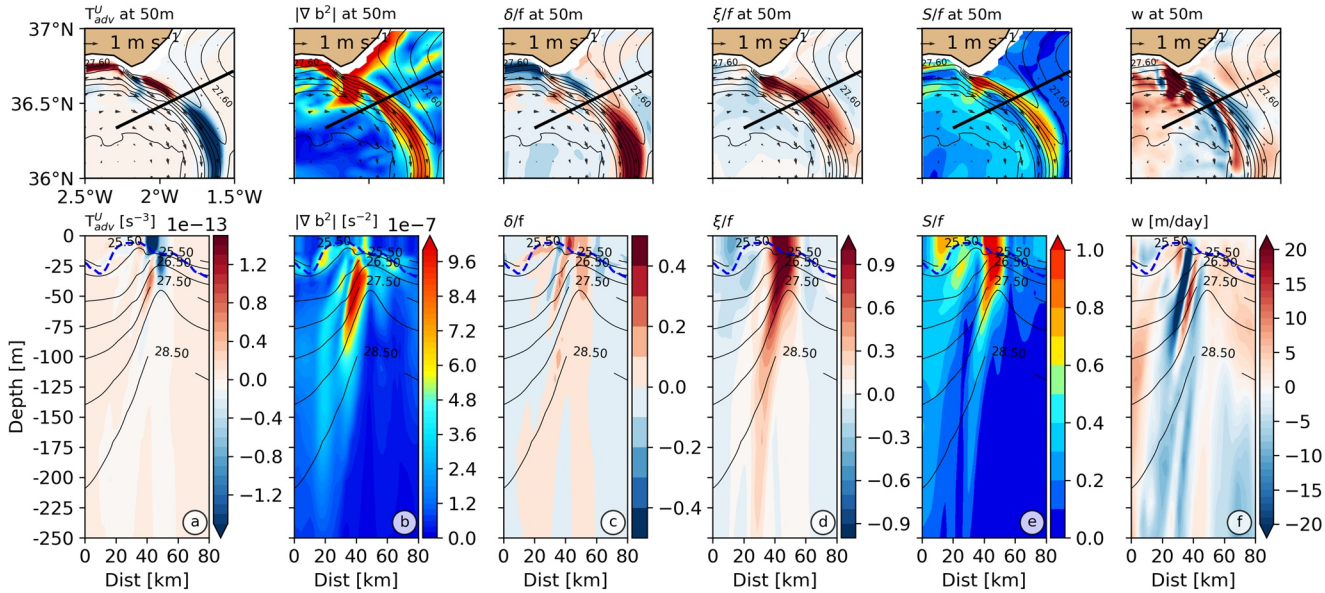

Figure 6. Diagnosis of the frontogenesis mechanism in the Eastern Alboran Gyre Front on 2 July 2018 from Western Mediterranean OPerational system daily averaged simulation. Map at 50 m depth and vertical structure: (a) advective frontal tendency, (b) lateral buoyancy gradient, (c) horizontal divergence, (d) vertical relative velocity, (e) horizontal strain rate, and (f) vertical velocities. In the maps, the potential density anomaly contours (black lines, contour interval is 0.2 kg m^{-3}) and the section by the black line are also displayed. The black vectors show the 100 m depth currents. In the vertical sections, the solid black lines indicate the position of the isopycnals. The blue dashed line shows the mixed layer depth diagnosed as the depth at which the density exceeds the surface density by 0.05 kg m^{-3}.

and divided into a light and a dense side. The vertical extent is confirmed by the depth extension of the horizontal buoyancy gradients and the positive T^U_{avd}. However, negative T^U_{avd} is observed in the upper ocean suggesting a weakening of the front and of the buoyancy gradients. On the other hand, the correspondence between divergence, relative vorticity, and horizontal strain rate fields associated with the AJ suggest that cyclonic vorticity grows in the presence of a convergence flow ($\delta < 0$) on the dense side of WAGF, developing strong downwelling. This convergence region (map Figure 5c) is also observed in the AJ located on the dense side of the front upstream of the plotted section, generating strong downwelling downstream (map Figure 5f). The convergence on the dense side of the front amplifies the cyclonic relative vorticity, leading to stronger cyclonic vorticity on the denser side than the anticyclonic vorticity on the lighter side (Figure 5d). Mahadevan and Tandon (2006) provide an explanation for the preponderance of cyclonic vorticity based on the fact that the rate of change of absolute vorticity is proportional to convergence. When $Ro \sim \mathcal{O}(1)$ in the frontal region, the growth of vorticity is asymmetric, and for the case $\xi > f$ cyclonic vorticity grows in the presence of a convergence region, whereas anticyclonic vorticity decays.

Finally, the frontogenesis patterns are associated with large vertical velocities that are particularly intensified in the downward direction. In the Alboran Sea simulation, upward velocities (light side) are much weaker than downward velocities (heavy side). The daily averaged maximum of upward velocities is +20 m/day at 60 m on the light side, and the daily averaged maximum downward velocities is −55 m/day at 150 m depth below the mixed layer depth. This difference between upward and downward velocity magnitudes is consistent with the theory of ageostrophic motion contribution (Mahadevan, 2016; McWilliams, 2016). The WAGF intensification is consistent with the strain-induced frontogenesis mechanism, which forms a large subduction region developing a strong negative vertical velocity in the dense side below the mixed layer depth, associated with the meandering of the AJ.

4.2.2. EAG Front

In the EAG front region, the Hovmöller diagram obtained from the EAGF section shows the intensification of the vertical velocities on 2 July 2018 at 50 m depth (Figure 4b). The vertical velocity magnitude increase is associated with the increase of horizontal salinity gradients leading to isopycnal convergence (magenta lines). The indicators of frontogenesis across the EAGF obtained from WMOP simulation are presented in Figure 6. The vertical structure of the density across the EAGF is characterized by a bell-shaped curve profile, with a local pointy density in

the frontal region. Additionally, in the EAGF large lateral buoyancy gradients are observed down to 100 m depth, associated with a positive T^{U}_{avd}. On the other hand, the plan views show complex and hectic meso- and submeso-scale activities in the EAG region characterized by meanders, vortices, and filaments. A relevant feature is the penetration of an intense and elongated meander to the Mediterranean Sea, characterized by a mostly positive T^{U}_{avd} in the upstream meander, a large strain rate and an intense cyclonic relative vorticity that are associated with a convergence region.

The vertical profiles of the diagnostic variables of the frontogenesis mechanism show maximum values which reach down to 100 m. The intense vertical structures of the strain rate and cyclonic relative vorticity take place where the lateral buoyancy gradient is intensified. According to the frontogenesis theory, the generation of significant horizontal (density and velocities) gradients produce upward velocities on the light side and downward on the heavy side of the front by ageostrophic motion. However, the vertical profile of the vertical velocities shows a varied and complex pattern characterized by the upward velocities between cells with large downward velocities (−38 m/day at 40 m depth), as it is observed in the center of the front. This pattern has been observed in the previous and the following days, and it is produced by the presence of a cold filament associated with the AJ in the EAGF region, as it is illustrated in Figure 1b. Summarizing, the EAGF is associated with a cold filament, and the sharp structure of the front is characterized by pointy density contours, a complex pattern of vertical velocities, and a shallow subduction region. Therefore, the strain-induced frontogenesis mechanism does not fully explain the development of vertical velocities in the front.

4.3. Instability Processes

An alternative mechanism that explains vertical velocities and (sub)-mesoscale structure developments are instability processes. In this section, we diagnose whether conditions are favorable for (sub)-mesoscale instability growth during the period of vertical velocities intensification by the frontogenesis mechanism in the regions of WAGF and EAGF. Using the Alboran Sea simulation output and CALYPSO 2018 glider observations, the potential role of (a) SI, (b) ageostrophic anticyclonic baroclinic instabilities, and (c) gravitational instability (convection) are evaluated by (a) the change of sign of EPV (Adams et al., 2017; Thomas et al., 2013; Thompson et al., 2016; Viglione et al., 2018), (b) the difference between absolute vorticity and strain rate ($A - S$; Molemaker et al., 2005), and (c) the vertical buoyancy gradient or stratification (N^2; Mahadevan & Tandon, 2006).

The EPV is a diagnostic tool to identify conditions that lead to flow instabilities: the flow is unstable when EPV is of the opposite sign of the Coriolis parameter, that is, EPV is less than zero in the Northern Hemisphere (Hoskins, 1974; Haine & Marshall, 1998; Thomas & Ferrari, 2008). The three-dimensional EPV is defined as follows.

$$\begin{aligned} \mathrm{EPV} &= (f\mathbf{k} + \nabla \times \mathbf{u}) \cdot \nabla b, \\ &= \boldsymbol{\omega_a} \cdot \nabla b, \\ &= (w_y - v_z)\, b_x + (u_z - w_x)\, b_y + (f + \xi)\mathrm{N}^2, \end{aligned} \tag{4}$$

where the absolute vorticity $\boldsymbol{\omega}_a = f\mathbf{k} + \nabla \times \mathbf{u}$ is the sum of planetary and relative vorticity, f is the Coriolis parameter, $\mathbf{k}$ is the vertical unit vector, ∇ the gradient operator, $\mathbf{u}$ is the three-dimensional fluid velocity, b is the buoyancy, defined as $b = g\rho'/\rho_0$, where g is the gravitational acceleration, the perturbation density ρ' is measured as density minus the reference density $\rho_0 = 1{,}027.15$ kg m^{-3}, f is the Coriolis parameter, $\xi = v_x - u_y$ is the vertical relative vorticity, and $N^2 = b_z$ is the vertical stratification. x and y subscripts indicate partial differentiation in the zonal component and meridional direction, respectively.

The EPV is generally positive in the Alboran Sea because fN^2 is positive and dominates the EPV (Equation 4). However, the EPV can become negative when the fluid column: (a) is unstably stratified (gravitational instability), (b) experiences horizontally sheared flow (inertial or centrifugal instability), and (c) strong lateral buoyancy gradients (SI; Thompson et al., 2016). On the one hand, if lateral variations in velocity and buoyancy are small, EPV may be negative if the flow is unstably stratified or $N^2 < 0$, which gives rise to gravitational instability. The active mixing region produces gravitational instabilities associated with change of sign of vertical buoyancy gradient or N^2 (Mahadevan & Tandon, 2006; Molemaker et al., 2005). On the contrary, as horizontal buoyancy gradients (b_x, b_y) and horizontal vorticity ($w_y - v_z$, $u_z - w_x$) become stronger, additional terms must be considered,

which gives rise to a baroclinic component. Accordingly, the horizontal vorticity can be a negative quantity that lowers EPV.

The observations from a single glider are restricted to a vertical and a single horizontal dimension, therefore we used an observational vertical vorticity and EPV in two-dimensions assuming a two-dimensional and hydrostatic flow that does not vary in the along-front direction. By assuming that the vertical velocities are smaller than the horizontal velocities, the horizontal gradient of the vertical velocities involved in EPV Equation 4 are neglected. Additionally, the vertical vorticity and EPV were computed neglecting dx terms in Equation 4 by assuming that along-front gradients are much smaller than the cross-front gradients (the local coordinates are x' and y' in the along- and cross-front direction) and that the gliders were piloted perpendicular to the fronts. Under these approximations, the frontal vertical vorticity is $\xi_{obs} = -u_{y'}$ and the observational EPV ($\mathrm{EPV_{obs}}$) is defined by:

$$\begin{aligned} \mathrm{EPV_{obs}} &= \left(0, u_z, f - u_{y'}\right) \cdot \left(0, b_{y'}, b_z\right), \\ &= u_z b_{y'} + \left(f + \xi_{obs}\right) b_z. \end{aligned} \tag{5}$$

In addition, the comparison of the observational and full EPV for different angles between the front and virtual glider sections are presented in Appendix A. The analysis shows that an oblique angle produces an elongation of the EPV pattern associated with an underestimation of the EPV magnitude, but does not affect the EPV change of sign in the frontal region, which is related to the conditions for instabilities.

Moreover, to investigate the nature of frontal instabilities, the diagnostics of energetic analysis are calculated in the presence of frontogenesis using outputs of Alboran sea simulation. SI can extract kinetic energy from geostrophic flows to perturbation kinetic energy at a rate given by the geostrophic shear production (GSP; Bachman et al., 2017; Gula et al., 2014; Jing et al., 2021) as

$$\mathrm{GSP} = -\overline{\mathbf{u}' w'} \frac{\partial \overline{\mathbf{u_g}}}{\partial z}, \tag{6}$$

where the overline and primes denote a spatial average and the deviations from a cross front average, respectively; $\mathbf{u_g}$ refers to the geostrophic flow. The geostrophic component is determined based on the thermal wind balance $\left(f\mathbf{k} \times \frac{\partial \mathbf{u_g}}{\partial z} = -\nabla_h b\right)$. Furthermore, conversion from available potential to perturbation kinetic energy conversion that is leading to ageostrophic baroclinic instability is quantified by the vertical buoyancy flux (BF),

$$\mathrm{BF} = \overline{w' b'}, \tag{7}$$

where w' and b' is the vertical velocities and buoyancy deviation from a cross front average, respectively. $\mathrm{BF} > 0$ corresponds to restratification of the front. Finally, the GSP and BF represent downscale energy transformation from the mean flow to the variable part and are an identified source for SI and ageostrophic baroclinic instability. According to Bachman et al. (2017), the SI growth horizontal length scales is estimated by $L_{SI} = 2\left(\frac{\mathrm{U}}{f}\right)\sqrt{1 - \mathrm{RI_b}}$, with $U = 1$ m/s and $RI_b = 0.95$, we obtain a spatial scale of SI at the frontal region of the Alboran Sea of the order of 4,700 m. This is more than twice the WMOP model grid spacing (2,000 m). While SI can certainly not be fully resolved by this resolution in the absence of specific parametrizations, they can still be represented by the model.

Summarizing, a negative EPV which tends to destratify the mixed layer (low Ri) can be generated by a strong thermal wind shear in sharp frontal regions (Mahadevan, 2016). Negative EPV gives rise to SI or gravitational instability (Taylor & Ferrari, 2009), which restores EPV to a neutral state (EPV = 0) by restratification over a few inertial periods. The condition for ageostrophic anticyclonic baroclinic instabilities are evidenced by the difference between absolute vorticity and strain, $A - S = (f + \xi) - S$. Negative regions in $A - S$ show that a loss of diagnostic force balance is occurring in the vicinity of the frontal region (Molemaker et al., 2005).

4.3.1. WAG Front

To identify the location where instabilities processes play a potential role in the development of the vertical velocities, the physical properties: EPV, $A - S$, N^2, and Ri obtained from the Alboran Sea simulation are plotted in Figure 7. These quantities correspond to the WAGF region on 12 June 2018, and were calculated using 3D fields from the WMOP outputs. The 3D EPV was computed as in Equation 4. In the plan views, the near surface

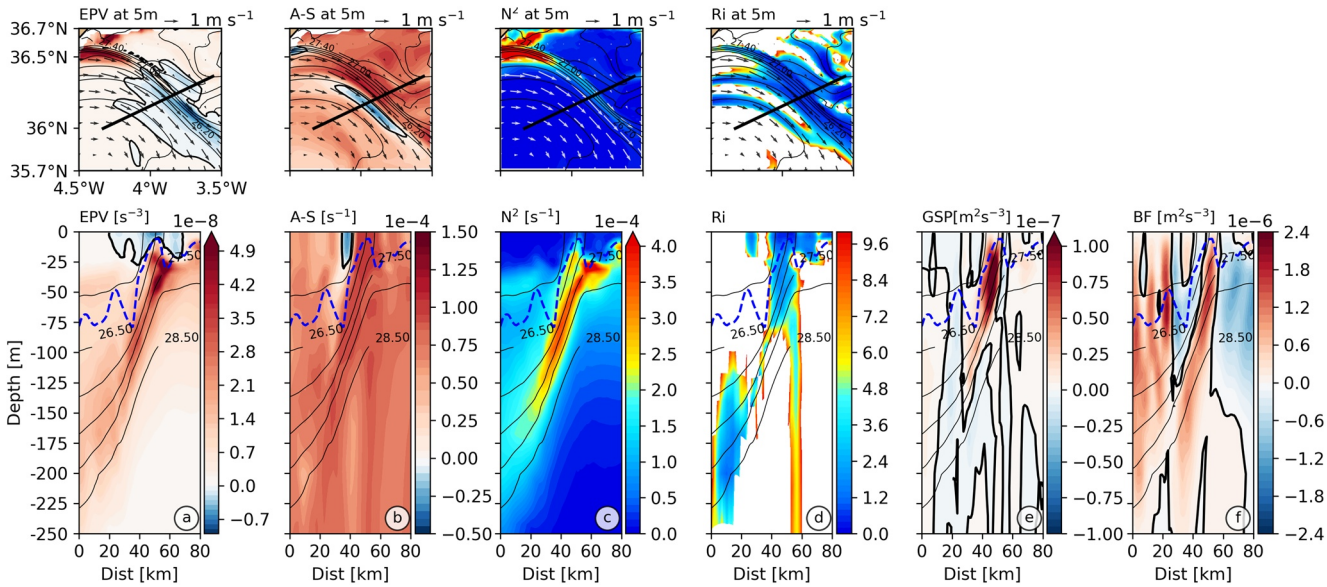

Figure 7. Diagnostics of instabilities processes in the Western Alboran Gyre Front on 12 June 2018 from Western Mediterranean OPerational system daily averaged simulation. Plan views at 5 m and vertical sections of (a) the Ertel potential vorticity (Equation 4), (b) $A - S$, (c) vertical stratification (N^2), (d) Richardson number (Ri), (e) geostrophic shear production, and (f) vertical buoyancy flux. The front cross-section is indicated with a black line and the potential density anomaly contours (thin black lines, contour interval is 0.2 kg m^{-3}) in the plan view. Ri range is 0–10 (higher values are not plotted). The blue dashed line shows the mixed layer depth diagnosed as the depth at which the density exceeds the surface density by 0.05 kg m^{-3}.

values at 5 m depth of EPV, $A - S$, and N^2 are predominately positive and the site where EPV and $A - S$ change sign coincides with the WAGF. Additionally, a correspondence is observed between regions of sign change and low Ri. Such conditions favor the occurrence of instabilities in the WAGF and indicate submesoscale processes activity with development of vertical velocities. Small and positive N^2 (Figure 7c) is observed around the WAGF without sign change, suggesting the presence of a weakly stratified region. Additionally, the low Ri (Figure 7d) in the region indicates that the WAGF region satisfies the conditions for symmetric instabilities generation and a loss of balance motion associated with submesoscale structures.

In Figure 7, while the vertical structure shows the shallowness of the mixed layer (down to 25 m) at the front's denser side; a deepening of the mixed layer (down to 75 m) occurs on the light side of the front, where instabilities can arise in the mixed layer if conditions are satisfied. The sign change of EPV and $A - S$ are located in the mixed layer at around 30 m depth in the less dense region of the WAGF. Upwelling velocities are associated with the near surface sign change region. Therefore, the symmetric instabilities produced by the EPV sign change and $Ri < 1$ are located in the upper ocean, suggesting that they are associated with submesoscale surface structures. However, the $A - S$ is highly variable down to 100 m depth and coincides with downwelling velocities. The high variability and sign change regions of $A - S$ in Figure 7b generate a loss of geostrophic balance along the front and give rise to an ASC across the section of the front, providing favorable conditions for the development of ageostrophic anticyclonic baroclinic instabilities. The large positive values of EPV, $A - S$, N^2, and high Ri are located in the dense side of the front below the mixed layer, and they are associated with higher downwelling motion. In turn, the large downwelling velocities coincide with regions of important strain, associated with the jet meandering produced by a baroclinic instability. Moreover, during the frontal intensification, the diagnostic across the WAGF section of GPS (Equation 6) and BF (Equation 7) are presented in Figures 7e and 7f. The values of BF are the dominant source of energy for the perturbation by an order of magnitude than GSP values. The large positive GSP and BF in the sharp density contour in the WAGF area suggest an efficient conversion from geostrophic flows to submesoscales. The positive GSP in the mixed layer and associated sign change regions of EPV (Figure 7a) identify favorable conditions for SI in the mixed layer in the WAGF zone. Meanwhile, below the mixed layer the positive GSP and BF suggest the occurrence of baroclinic and ageostrophic baroclinic instabilities.

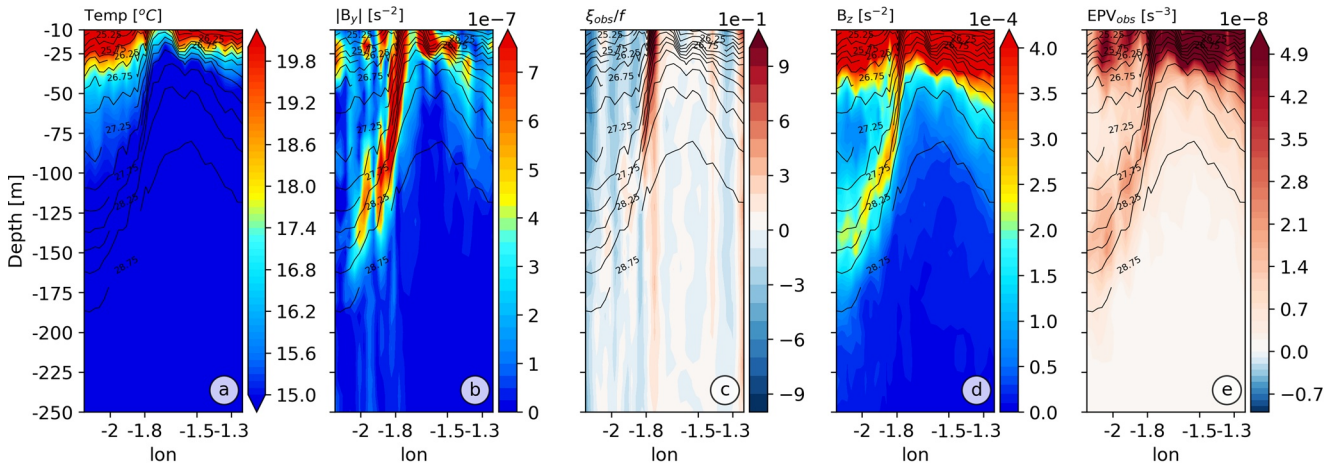

Figure 8. Diagnostics of frontogenesis mechanism and instabilities processes in the Eastern Alboran Gyre Front from sp56 glider data from 5 July to 10 July. Vertical section of (a) the temperature, (b) the lateral buoyancy gradient, (c) observational relative vorticity, (d) vertical stratification, and (f) observational Ertel potential vorticity (Equation 5). Isopycnals are indicated by black lines (contour interval is 0.25 kg m^{-3}).

In summary, the WAGF region satisfies the condition to generate symmetric and ageostrophic baroclinic instabilities above the mixed layer associated with upwelling velocities. Meanwhile, baroclinic instabilities below the mixed layer lead to intense downwelling velocities across the section of the front.

4.3.2. *Glider Observations in EAG Front*

The frontogenesis and instabilities processes in the EAGF are first investigated here from glider observations to provide an observational counterpart to our model analysis. The diagnostics from sp56 glider data from 5 to 10 July show an EAGF intensification as it is indicated by the vertical profiles of the temperature, lateral buoyancy gradient, relative vorticity, stratification, and EPV_{obs} (Equation 5). A similar pattern was found in sp59 glider trajectory on 5–11 July (figure not shown).

The temperature (Figure 8a) suggests an incoming cold meander near the surface and a shallow mixed layer. The lateral buoyancy gradient (Figure 8b) shows the front intensification produced by a pointy density contour. The extension of the front captured by $|\nabla b^2|$ indicates a depth of 150–180 m and a width of 10–40 km. The relative vorticity (Figure 8c) shows features of the frontogenesis theory, which are the predominance of cyclonic vorticity on the front's denser side and the predominance of anticyclonic vorticity on the lighter side. The relative vorticity leads to a local $Ro \sim \mathcal{O}(1)$ in the front indicating submesoscale processes activity and the influence of ASC on the vertical velocities. The pointy and bell-shaped density contours are characteristic of the filamentogenesis processes (see Section 4.5). The density contour pattern indicates the intrusion of Atlantic waters from the north, as it is illustrated in Figure 1b and SST satellite images from Zarokanellos et al. (2022). Figure 8d shows a high stratification in the upper ocean and in the sharp front, and a shallow mixed layer from the surface to 40 m depth. As the stratification does not show any sign change, the condition for gravitational instabilities generation is not satisfied. The EPV_{obs} (Figure 8e) also shows high values in the upper ocean and in the sharp front; but these data does not allow to evidence any EPV_{obs} sign change depicting conditions for symmetric instabilities.

Summarizing, the satellite images of the Alboran Sea (Figure 1b) and the temperature from sp56 glider (Figure 8a) show the EAGF associated with a cold sharp filament that introduces Atlantic water to the eastern part of Alboran Sea, which then flows into the Mediterranean Basin. The glider observations in the EAGF shows (a) submesoscale activity that generates ageostrophic motion, which influence the vertical velocities development, and (b) a strong stratification in the upper ocean and a shallow mixed layer, that inhibit the conditions for instabilities processes generation. A more detailed analysis of the multiple CALYPSO glider data is provided in Zarokanellos et al. (2022).

4.3.3. *WMOP Simulation in EAG Front*

The diagnostics of the conditions for instabilities processes in the model in the EAGF region on 2 July 2018 are pointed in Figure 9. The WMOP simulation shows a 30 km offset in the position of the EAGF as previously indi-

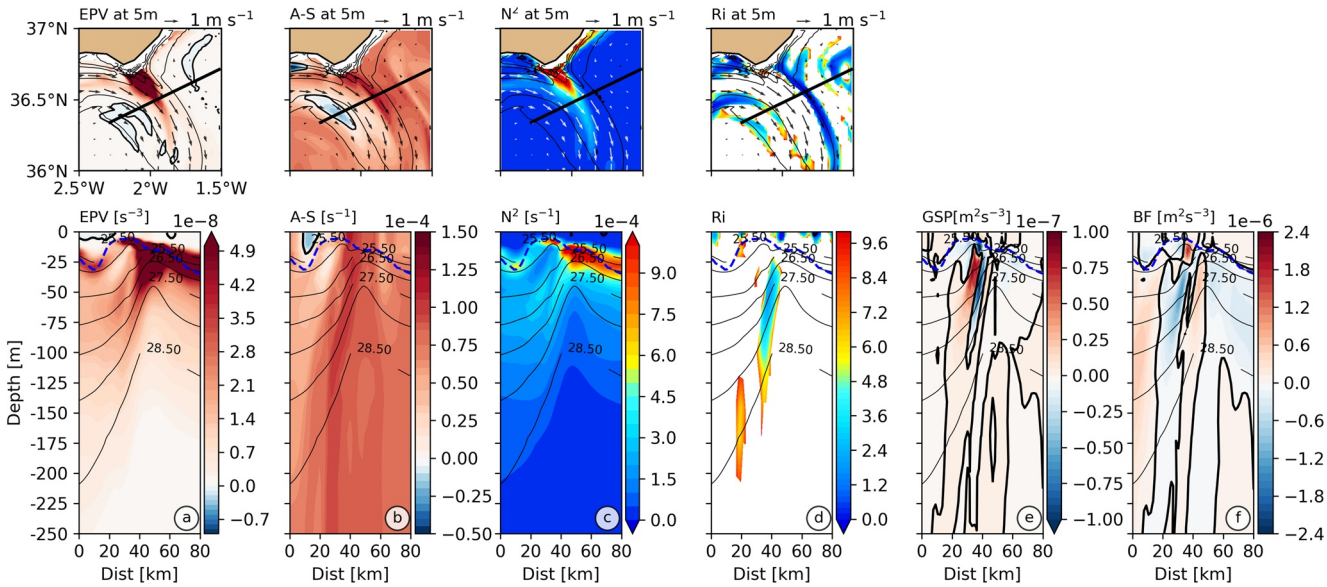

Figure 9. Diagnostics of instabilities processes in the Eastern Alboran Gyre Front on 2 July 2018 from Western Mediterranean OPerational system daily averaged simulation. Plan views at 5 m and vertical sections of (a) the Ertel potential vorticity (Equation 4), (b) $A - S$, (c) vertical stratification (N^2), (d) Richardson number (Ri), (e) geostrophic shear production, and (f) vertical buoyancy flux. The front cross-section is indicated with a black line and the potential density anomaly contours (thin black lines, contour interval is 0.2 kg m^{-3}) in the plan view. Ri range is 0–10 (higher values are not plotted). The blue dashed line shows the mixed layer depth diagnosed as the depth at which the density exceeds the surface density by 0.05 kg m^{-3}.

cated (Section 3.2). However, the model satisfactorily represents the horizontal and vertical structure of the sharp front. The plan views, at 5 m depth show the predominantly positive values of EPV, $A - S$, and N^2 in the vicinity of the EAG region. However, there are also regions downstream of the EAGF section, where the sign change of EPV and $A - S$ are observed. Both EPV and $A - S$ are associated with a weak stratification and low Ri. Therefore, the regions of sign change satisfy the condition for occurrence of the symmetric and ageostrophic anticyclonic baroclinic instabilities associated with submesoscale surface structures.

The vertical structure shows that the EPV and $A - S$ vertical profiles (Figures 9a and 9b) in the EAGF section show a region of sign change above the mixed layer (≈25 m depth), which is located on the lighter side of the front. This region overlaps with areas of weak stratification and low Ri (Figure 9d), permitting an EPV change of sign. This suggests that the favorable conditions for SI evidenced by the GSP positive region at the surface in the beginning of the section in Figure 6e are produced by an intense vertical mixing in a shallow mixed layer (Thomas & Lee, 2005; Mahadevan & Tandon, 2006). The sign change region above the mixed layer coincides with a weak downwelling region downstream of the EAGF section (Figure 6e).

On the other hand, the regions of higher EPV, $A - S$, and Ri values coincide with the emerging of an intense downwelling region in the center of EAGF (Figure 6e). This downwelling region is between upwelling regions indicating a complex ASC across the front. Meanwhile, the slope of the isopycnals steepens and generates large lateral buoyancy gradients, which induce baroclinic instabilities that lead to the frontal jet meandering. BF is the dominant conversion term. We observe a larger positive GPS (Figure 9f) and BF (Figure 9e) patterns below the mixed layer, indicating the preponderance of baroclinic and ageostrophic baroclinic instabilities in the frontal area and an efficient conversion of geostrophic KE and frontal APE to submesoscale flow. Simultaneously, vertical velocities are developed below the mixed layer.

Summarizing, the comparison with the glider observations in the EAGF indicates that WMOP simulation captures satisfactorily the frontal and submesoscale dynamics, as depicted by the variability of local Rossby number $\mathcal{O}(1)$ in the frontal region. The EAGF shows that the conditions for sign change of EPV and $A - S$ are satisfied on the lighter side of the front above the mixed layer. As a result, SI and ageostrophic anticyclonic baroclinic instabilities can be generated at these locations and associated with an intense superficial submesoscale activity. Furthermore, at the front's center and below the mixed layer the lateral buoyancy gradients trigger baroclinic instabilities.

Finally, the instabilities processes observed in the EAGF are linked to a complex ASC characterized by a downwelling region between upwelling regions.

4.4. Nonlinear Ekman Effects

In this section, the influence of the down-front winds on the frontogenesis process and therefore on the development of vertical velocities produced by an ASC is analyzed. Wind stress acts on fronts through nonlinear Ekman transport and destruction of EPV (Thomas, 2005; Thomas & Lee, 2005; Mahadevan & Tandon, 2006; Pallàs-Sanz et al., 2010). The ocean front submitted to a wind blowing in the direction of the frontal jet extracts EPV from the Ekman layer producing a subduction of low EPV water and a cross-front advection of density by Ekman transport. Therefore, an exchange of low EPV from the Ekman layer and high EPV from the pycnocline occurs driven by an ASC (Thomas, 2005). Additionally, Thomas and Lee (2005) suggested that along-front winds can generate intense downwelling due to cross-front Ekman transport at the surface. This transport drives dense water over light water, resulting in ASC cells that feedback upon themselves and enable exchange with deeper waters. Therefore, the ASC is characterized by subduction on the dense side of the front and upwelling along the front. Finally, the nonlinear Ekman current induced by the wind in the upper ocean drives the frontogenesis process (Capet et al., 2008) and generates an ASC (Pallàs-Sanz et al., 2010).

The nonlinear Ekman transport ($\boldsymbol{\mathcal{M}_E}$) is normal to the wind stress and is modulated by the absolute vorticity at the surface as follows

$$\boldsymbol{\mathcal{M}_E} = -\frac{\mathbf{k}\times\boldsymbol{\tau}^{\mathrm{h}}}{\rho_0(f+\xi)}, \tag{8}$$

where $\boldsymbol{\tau}^h$ is the horizontal component of the wind stress. The Ekman pumping velocity is obtained from the divergence of the Ekman transport. Then, the full Ekman vertical velocities ($\mathcal{W}_E$) formed by the linear and nonlinear components from the rotational of the wind stress and divergence of the relative vorticity, respectively, is as follows:

$$\begin{aligned}\mathcal{W}_E &= \frac{1}{\rho_0}\nabla_{\mathrm{h}}\cdot\boldsymbol{\mathcal{M}_E},\\ &= \frac{\mathbf{k}}{\rho_0(f+\xi)}\cdot\nabla_{\mathrm{h}}\times\boldsymbol{\tau}^{\mathrm{h}} + \frac{\mathbf{k}\times\boldsymbol{\tau}^{\mathrm{h}}}{\rho_0(f+\xi)^2}\cdot\nabla_{\mathrm{h}}(f+\xi),\\ &= \frac{1}{\rho_0(f+\xi)}\left(\tau^y_x-\tau^x_y\right) + \frac{1}{\rho_0(f+\xi)^2}\left(\tau^x\xi_y-\tau^y\xi_x\right),\end{aligned} \tag{9}$$

where τ^x and τ^y are the eastward and northward components of the wind stress, ρ_0 is the reference density, and ξ is the relative vorticity. Therefore, the Ekman vertical velocities induce up- and down-welling regions in the Ekman layer and contribute to the development of the vertical velocity at the vicinity of the frontal region (Mahadevan & Tandon, 2006; Mahadevan et al., 2008).

The Ekman layer depth (δ_E) is approximated by $\delta_E = 0.4\frac{u^*}{f}$, where the frictional velocity is $u^* = \sqrt{\frac{|\boldsymbol{\tau}^{\boldsymbol{h}}|}{\rho_0}}$ (Mahadevan & Tandon, 2006). The wind speed at 10 m ($W_{10} = |\boldsymbol{U_{10}}|$) is obtained from the HIRLAM model used to force the WMOP simulation (Section 3.2). The surface wind stress is obtained from the bulk formula: $\boldsymbol{\tau^h} = (\tau^x, \tau^y) = \rho_{air}\, C_d\, W_{10}\, \boldsymbol{U_{10}} = \rho_{air}\, C_d\, W_{10}\, (u_{10}, v_{10})$, where W_{10}, u_{10}, and v_{10} are the wind speed at 10 m and its zonal component and meridional component, respectively. The density of air is given by ρ_{air} and is approximately equal to 1.22 kg m^{-3}, and C_d is the neutral drag coefficient computed as $C_d = 4.9\cdot10^{-4} + 6.5\cdot10^{-5}\,|\boldsymbol{U_{10}}|$, for wind speeds larger than 10.15 m s^{-1} (Large & Pond, 1981).

In the following sections the nonlinear Ekman effects observed in the WAGF and EAGF are shown in Figures 10 and 11. The daily mean values presented correspond to the dates associated with vertical velocities development selected from the Hovmöller diagrams (Figure 4).

4.4.1. WAG Front

In the western region, Figures 10a–10c show the nonlinear Ekman transport ($\boldsymbol{\mathcal{M}_E}$), which is normal to the right of the wind direction. The period 05 to 12 of June shows persistent down-front winds blowing in the direction of the frontal jet that is, westward direction leading to southward Ekman transport. The advection of the dense

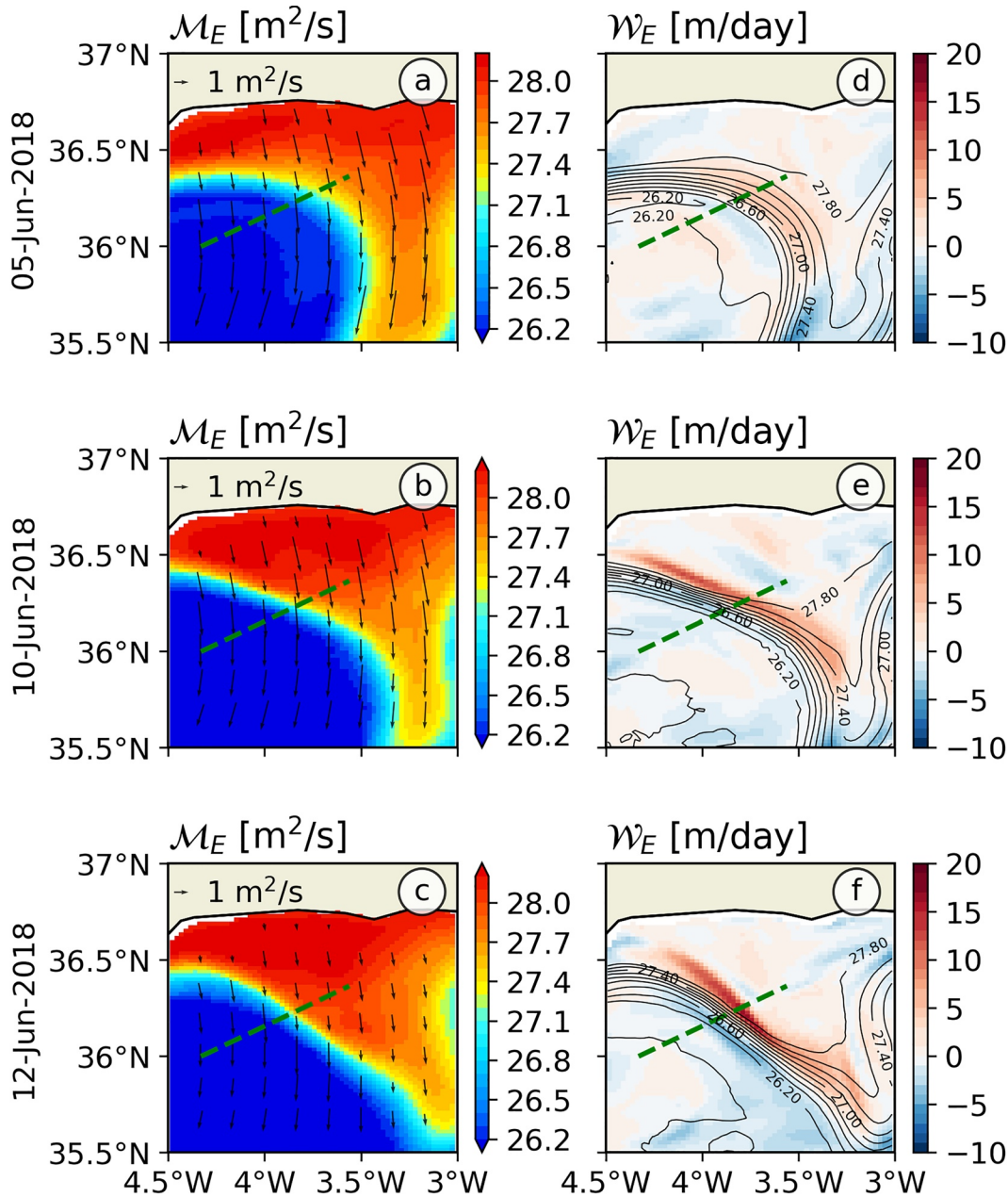

Figure 10. Diagnosis of the nonlinear Ekman effects evaluated on 5, 10, and 12 June from Western Mediterranean OPerational system daily averaged simulation in the Western Alboran Gyre Front region. Left: vector fields of nonlinear Ekman transport ($\mathcal{M}_e$) over the surface potential density anomaly field, and right: plan-view of nonlinear vertical Ekman velocities ($\mathcal{W}_e$) and surface potential density anomaly (black lines, contour interval is 0.2 kg m^{-3}). The green dashed line indicates Western Alboran Gyre Front section.

water across the front has a unbalancing effect on the water column and generates a negative BF on the light side of the front. The cross-front Ekman transport starts at the Ekman layer, which depth is approximately 53 m, a similar depth was reported by Oguz et al. (2017). The Ekman transport develops a downwelling region of about $\mathcal{W}_E = -4.1$ m/day found in the vicinity of the frontal jet and an upwelling region of $\mathcal{W}_E = +15.5$ m/day the dense side (Figure 10e). The Ekman transport drives dense water over the light side, resulting in ASC cells that feedback upon themselves and enable exchange from the Ekman layer to pycnocline. Furthermore, the down-front winds reduce the EPV in the whole upper ocean (Figure 7a), with a high-EPV on the dense side at the Ekman layer base and low-EPV on the light side of the front.

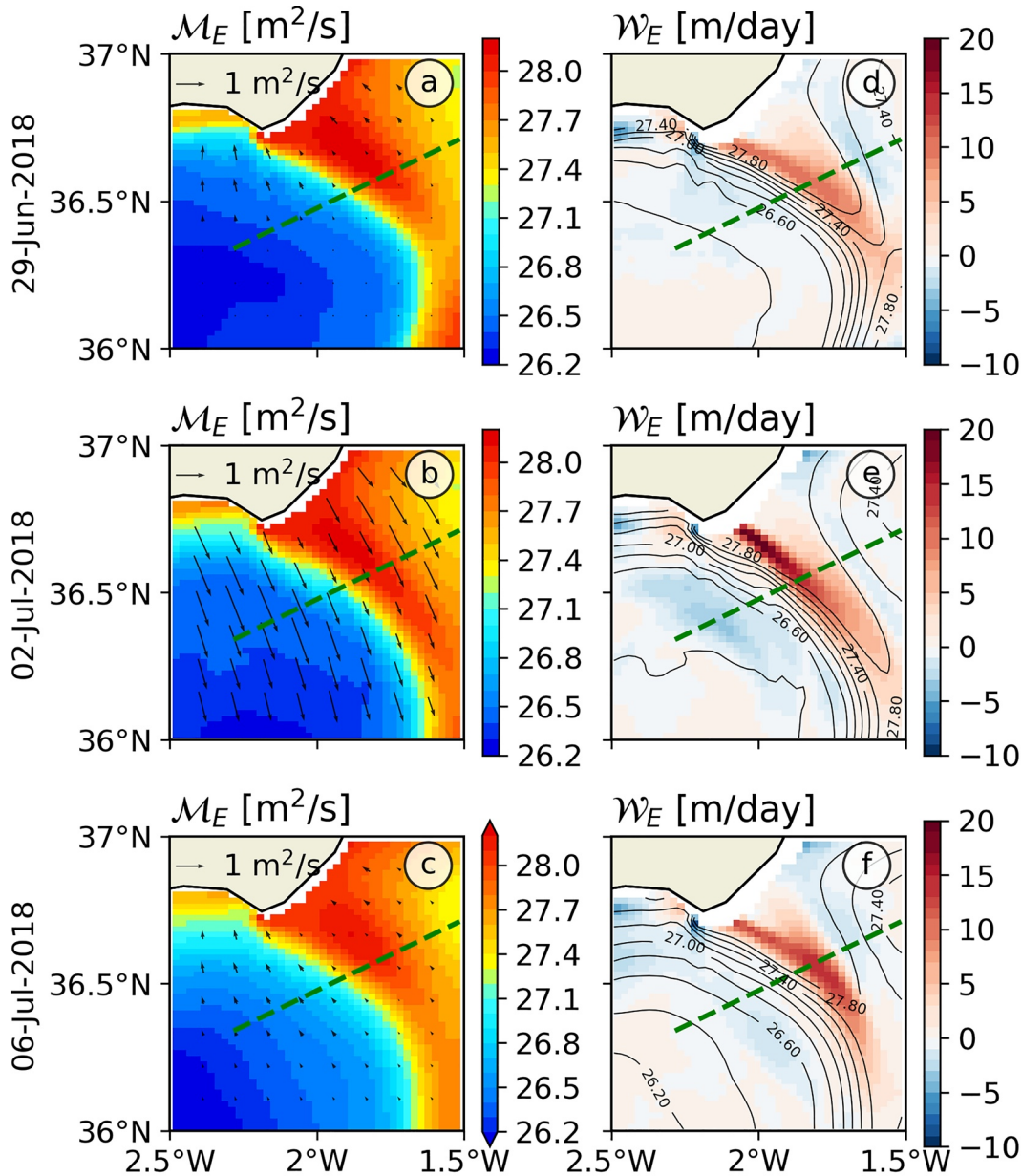

Figure 11. Diagnosis of the nonlinear Ekman effects evaluated on 29 June, 7 and 12 July from Western Mediterranean OPerational system daily averaged simulation in the Eastern Alboran Gyre Front (EAGF) region. Left: vector fields of nonlinear Ekman transport ($\mathcal{M}_e$) over the surface potential density anomaly field, and right: plan-view of nonlinear vertical Ekman velocities ($\mathcal{W}_e$) and surface potential density anomaly (black lines, contour interval is 0.2 kg m^{-3}). The green dashed line indicates EAGF section.

4.4.2. EAG Front

In the eastern region of the Alboran Sea, Figure 11 presents the diagnostic of Ekman effects evaluated on 29 June, 2 and 6 July. These dates correspond to the development of negative velocities observed in the Hovmöller from the EAGF section (Figure 4b). The arrows of $\mathcal{M}_e$ in Figures 11a–11c show a weak transport and high variability direction produced by changing winds over the region. The magnitude of $\mathcal{M}_e$ increases when a south-westward wind blows in the direction of the EAGF and produces the advection of dense water toward the light site of the front and generates an ASC. The Ekman layer depth in the EAGF region is approximately 16 m and the Ekman velocity suction ($\mathcal{W}_e$) is −1.73 m/day on the light side of the front (Figure 11e). Finally, on 2 July 2018 is the unique time when the Ekman transport satisfied the Ekman pumping by down-front winds. It is coincident with

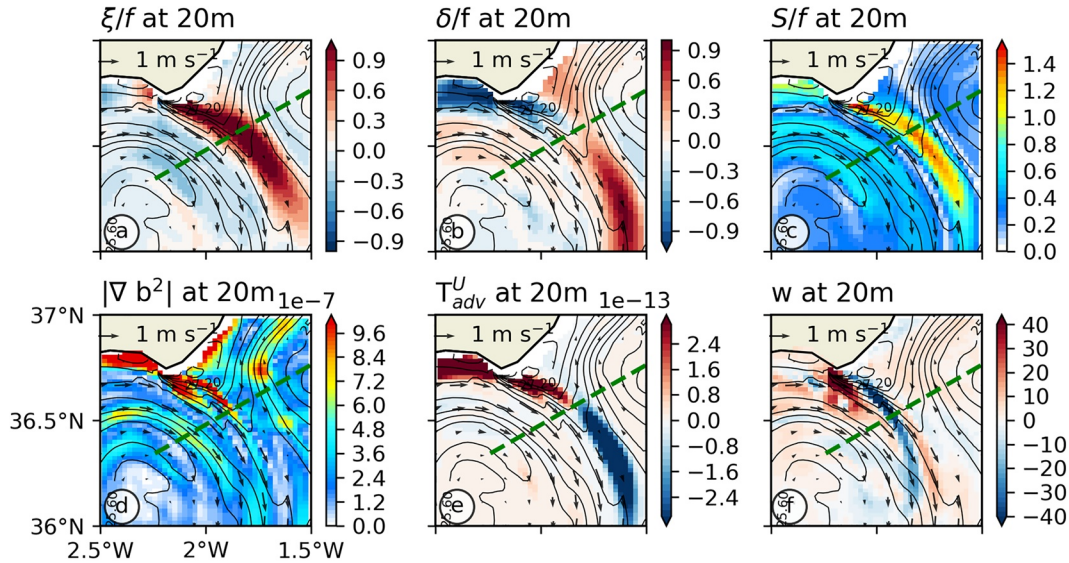

Figure 12. Diagnosis of filamentogenesis process in the Eastern Alboran Gyre Front region. Daily average (2 July 2018) horizontal patterns from Western Mediterranean OPerational system simulation at the 20 m depth of (a) vertical relative velocity, (b) divergence, (c) horizontal strain rate, (d) lateral buoyancy gradient, (e) advective frontal tendency (s^{-3}), and (f) vertical velocities (m/day). The frontal cross-section is indicated with a green line in the plan view. The black vectors show the 20 m depth currents. Potential density anomaly contours (black lines, contour interval is 0.2 kg m^{-3}) are also displayed.

the development of the downwelling velocities in the Hovmöller diagram of the vertical velocities in the EAGF (Figure 4b). Additionally, this wind regime can extract EPV from the ocean surface, making EAGF susceptible to SI, as indicated by the vertical profile of EPV in the EAGF section (Figure 9a).

4.5. Filamentogenesis Process

Vertical velocities in the EAGF are not fully explained by the strain-induced frontogenesis and instabilities processes. On the other hand, the Ekman process does not fully satisfactorily explain the vertical velocities intensification due to the high variability of the wind stress in the EAG region. In the present section, the role of the cold filaments in the intensification of the vertical velocities is investigated by the study of the filamentogenesis process in the EAGF. Filamentogenesis refers to filament frontogenesis, which indicates the intensification of fronts by a cold filament (Gula et al., 2014; McWilliams et al., 2009). In the EAGF, a cold and elongated filament penetrating to the interior of the Mediterranean Sea is observed in the SST image (Figure 1b) and glider observations (Figure 8a).

In the EAGF region, coherent submesoscale structures such as meanders, vortices, and filaments are observed in the model (maps in Figure 6). In this region, the intermittency of wind stress does not inhibit the generation of filaments, which are responsible for intensifying the front. This behavior is consistent with McWilliams et al. (2015) who showed that filaments evolution are not driven by the wind direction, and suggested that these submesoscale structures are highlighted with the $|\nabla\rho|^2$, $|\nabla b|^2$, and $|\nabla \boldsymbol{U}|^2$ terms. The development of vertical velocities observed in the Hovmöller diagram (Figure 4b) is not fully explained by the strain-induced frontogenesis process, but by a filamentogenesis mechanism derived from a single cold filament entering into the EAG region. Figure 12 shows the daily average patterns of several frontal diagnosis in the upper ocean (20 m depth) during the intensification of the EAGF by the filamentogenesis process on 2 July 2018.

Maps of relative vorticity, divergence, and strain rate show strong magnitudes at the ring of the EAG in Figures 12a–12c. The relative vorticity shows a cyclonic elongated filament and a convergence region associated with anticyclonic EAG circulation and cyclonic circulation in the northeast. Additionally, the submesoscale strain rate structure indicates a filamentogenesis mechanism acting on the sharp front. The front is located between the EAG and the northeast stream producing sharp gradients of buoyancy and velocities, which are identified by an elongated submesoscale filament structure (Figure 12d). The advective frontal tendency involved in the

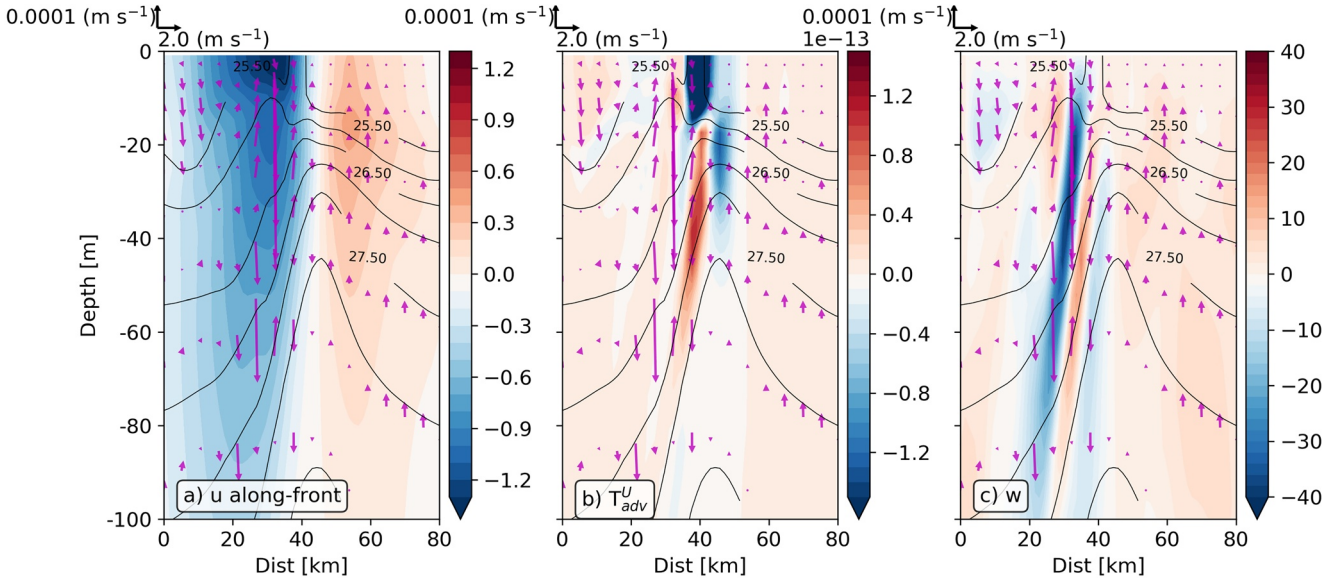

Figure 13. Daily average (2 July 2018) vertical patterns from Western Mediterranean OPerational system simulation of (a) along front velocities (m/s), (b) frontogenetic advection tendency term $\left(T^{U}_{avd}\right)$ (s^{-3}), and (c) the vertical velocities [m/day] during the Eastern Alboran Gyre Front (EAGF) intensification state along the EAGF section (Figure 12). Vertical and across-front velocities are indicated with magenta vectors. Potential density anomaly (black lines, contour interval is 0.2 kg m^{-3}) are also displayed.

filamentogenesis process is shown in Figure 12e, positive values indicate a frontogenesis mechanism upstream of the filament, which is evident by the sharp velocity gradient increase at the EAGF. On the contrary, negative values of T^{U}_{avd} indicate a frontolytic mechanism downstream of the filament, which is associated with a divergence region. The vertical velocity patterns observed in Figure 12f show an intense downwelling region along the frontal axis associated with a positive advective frontal tendency and coupled with an upwelling region on each side of the front. The observed pattern is consistent with that of a frontal intensification due to cold filaments (McWilliams et al., 2015). On other hand, the strong upwelling region near the Cape may be produced by the interaction of the upstream meander and the topographic features of the Spanish coast, as suggested by the sign change of relative vorticity (anticyclonic relative vorticity area [Figure 12a]) near the coast.

A vertical cross section of the EAGF (dashed green line in Figure 12a that corresponds to sp56 glider section) at the time of the filamentogenesis process is show in Figure 13. This figure shows the vertical structure of the density contours and the vertical and across-front velocities vectors. The center of the filament (1.8°W) coincides with dense and pointy density contours, which decay as they move away from the filament. In Figure 13a, the along front velocity contour is divided in two regions centered on the filament. One is located on the right side of the front and where the flow is southeastward in the direction of the front, associated with the anticyclonic EAG. The second region is located on the left side of the front and shows a northeastward flow associated with a cyclonic circulation in the northeast (Figures 12a–12c). The cross section of the advective frontal tendency (Figure 13b) shows that the largest values of T^{U}_{avd} are centered around the filament. The main frontolytic region is presented in the upper 10 m and a secondary weaker feature is found on the left side of the front. Then the frontogenetic advective tendency term is observed up to 70 m depth and presents maximum values at around 20 m depth, corroborated in the T^{U}_{avd} horizontal pattern (Figure 12e). This vertical structure of advection tendency is associated with the intensification of the buoyancy and velocity gradients (Figure 12d).

Finally, the vectors in Figure 13 and the vertical structure of the vertical velocities (Figure 13c) show the ASC that forms two re-circulation cells in each side of the filament, consistent with McWilliams et al. (2009). The secondary circulation restratify the flow and as a result the geostrophic balance is reestablished (Gula et al., 2014). The ASC generates vertical velocities on each side of the filament, upward on the dense side and downward on the light side, producing the sharpening of the isopycnals slope from the far side to the center of the filament indicating the introduction of light fluid toward the filament's center. The convergence of the flow at the surface (Figure 12b) gives rise to sharp downwelling velocities in the center of the filament. Instantaneous values of the

vertical velocity can reach $\mathcal{O}(100)$ m/day, as mentioned in Gula et al. (2014). However, the vertical structure produced by filamentogenesis observed in EAGF (Figure 13) is not symmetric as in the ideal case of filamentogenesis process, where the ASC cells have similar amplitude on each side. In the EAGF, the cells and frontogenesis in the advection tendency term are slightly shifted to the right. The asymmetry observed suggests that the filamentogenesis process does not act in the filament homogeneously in space as in the idealized scenario.

5. Discussions and Conclusions

The strong lateral salinity gradients, cold meanders, and frontal of the Alboran Sea regions were observed in satellite images and observations from UCTD and glider obtained during an intensive campaign carried out in Spring 2018 in the framework of the CALYPSO project. In this paper, the frontal intensification and development of the vertical velocities were specifically analyzed using a high-resolution free-run model simulation supported by high spatio-temporal observations. The CALYPSO 2018 campaign data acquisition came from multi-platform and high spatial-temporal resolution observations. In parallel, a WMOP free-run simulation was setup with 2 km spatial resolution, initialized from the outputs of the WMOP data-assimilative real-time forecast product at the beginning of the CALYPSO 2018 campaign.

The analysis of the evolution of the vertical velocities in the WAGF and EAGF using WMOP indicates different spatial-temporal frontal characteristics (see Hovmöller diagrams in Figure 4). The WAGF is wider, deeper, and longer-lasting than the EAGF. Additionally, the WAGF shows larger and deeper upwelling and downwelling regions than the EAGF. The different spatial-temporal variability observed in the fronts suggests that different mechanism drive frontal intensification and vertical velocities development in the WAGF and EAGF. The findings of the driving mechanism analysis in both fronts follow. In the WAGF region, the diagnostics for the strain-induced frontogenesis mechanism show a strong dominance of the AJ, suggesting it plays an important role in the WAGF intensification. The relevance of the AJ in the formation and extension of the WAG has been documented by Macías et al. (2008) and Oguz et al. (2016). At the same time, the westerly winds regime enhances the inflow of the Atlantic waters through the Gibraltar Strait, increasing the AJ velocity and displacing the jet toward the Spanish coast (Oguz et al., 2017).

The frontogenesis in the WAGF is produced by a horizontal density gradient intensification from the surface to 180 m depth in the presence of a large lateral strain rate, convergence, and cyclonic vorticity on the dense side of the front. Additionally, the frontogenesis mechanism is associated with a single ASC cell responsible to restore geostrophic balance. The ASC in the WAGF is characterized by upward velocities on the light side of the front, which are much weaker than the downward velocities on the dense side. In the EAGF region, the pattern of the diagnostics for the strain-induced frontogenesis mechanism are weaker and present shallower vertical structure (up to 100 m) than the WAGF. The WAGF intensification with the subsequent development of vertical velocities are well explained by an intense strain-induced frontogenesis mechanism driven by the AJ in the WAGF region. On the other hand, the vertical velocities profiles during the EAGF intensification show a more complex structure due to the action of the filamentogenesis process.

In terms of instability processes, Mahadevan and Tandon (2006) suggested that the gravitational, symmetric, and ageostrophic baroclinic instabilities can lead to vertical velocities development. The instabilities diagnostics during the WAGF intensification (12 June 2018) show a stronger and deeper signal of instabilities processes and mixed layer than the EAGF intensification. In the WAGF, the conditions for symmetric and ageostrophic baroclinic instabilities are satisfied on the light side of the front above the mixed layer, which are associated with submesoscale surface structures and upwelling velocities. In the meantime, baroclinic instabilities below the mixed layer produced by lateral buoyancy gradients lead to intense downwelling velocities. During the EAGF intensification (2 July 2018), the model indicates conditions for instability only below the shallow mixed layer in the frontal area as a consequence of a strong summer stratification (du Plessis et al., 2017; Thompson et al., 2016). Furthermore, the BF is the dominant source of energy for the perturbation below the mixed layer for WAGF and EAGF. This suggests that the preponderance of ageostrophic baroclinic instabilities in the frontal area and a more efficient conversion of frontal APE to submesoscale compared to geostrophic KE. Similar results of the preponderance of the baroclinic nature of submesoscale fronts are found by Capet et al. (2008) in the frontal instabilities analysis.

Both glider observations and the model indicate (a) weak frontogenesis mechanism features in the EAGF, that does not fully explain the front intensification; (b) submesoscale activity, which intensify the vertical velocities through the ASC contribution; (c) isopycnals slopes depicting a bell-shaped pattern, which indicate the intensification of the front through a cold filament; and (d) presence of strong lateral buoyancy gradients, indicating the generation of baroclinic instabilities below the mixed layer.

In the EAGF, contrary to the model, the glider observations suggest a lack of existence of instabilities in the upper ocean. Despite the fact that the conditions for instabilities generation are expected to be met, they are seldom captured by glider observations. The difficulty of the glider data to capture instabilities conditions has also been observed in the EAGF region by Ruiz et al. (2019). Reasons that complicate the observation of instabilities are (a) the unresolved hourly temporal variability of the mixed layer, and (b) the seldom occurrence of EPV change of sign, which is a condition required for symmetric instabilities generation. In this regard, the horizontal resolution grid of WMOP simulation can resolve the spatial scale of SI in the frontal area in the Alboran Sea, but the absence of specific parametrizations in the WMOP configuration may present some limitations (Dong et al., 2021). Negative EPV calculated from glider observation should not be as intense as in simulations due to the model tendency to overestimate EPV since it can not resolve the full range of SI, which is an important route for EPV to dissipate. However, the instabilities processes can be at least partially represented by the model, as suggested by the diagnostics of instabilities and energetic analysis. The precondition of EPV sign change is difficult to identify because EPV <0 is observed when $N^2 < 0$, a situation which occurs for instance when the mixed layer is deep and uniformly mixed. The summer stratification is more significant in the glider observations than in the WMOP simulation, also explaining why the conditions for instabilities generation are more difficult to identify in the observations. The only scenario when EPV changes sign is where N^2 is negative, also suggested in the simulation. Furthermore, the gravitational instabilities predominate over the symmetric instabilities in the EAGF and WAGF in the mixed layer. The instabilities show typical horizontal scales of a few kilometers ($\mathcal{O}$(1–10 km)) and temporal scales of the order of a day, in the presence of low *Ri* and large *Ro*. In contrast, the baroclinic instabilities grow below the mixed layer depth in the presence of large *Ri* and small *Ro*. Therefore, the presence of symmetric and baroclinic instabilities suggest that geostrophic kinetic and available potential energies are transferred to the variable flow, providing an interpretation for frontal energy dissipation (weaken the front), generate additional submesoscale features, and the amplification of the vertical velocities in the frontal area.

With respect to the Ekman effects, the down-front winds reduce ocean stratification (du Plessis et al., 2017; Mahadevan et al., 2008) and generate a negative EPV at the surface produced by wind frictional forces (Capet et al., 2008; Thomas & Lee, 2005). Furthermore, the nonlinear Ekman effects produce a cross-front Ekman transport at the surface generated by along front winds, and generates an intense downwelling. Thomas (2005) indicated that the along front wind generates downwelling produced by across-front Ekman transport at the surface. This transport drives dense water over the light side resulting in an ASC cell. In the WAG region, the wind blows in a cross-front direction constantly during the vertical velocities development producing a southward advection of dense water over the light water. Consequently, Ekman transport is produced and Ekman pumping velocity is generated, resulting in the intensification of both the WAGF and the cross-frontal ASC as reported by Oguz et al. (2017). In addition, the down-front winds effect is related to low-EPV waters on the light side of the front. On the other hand, the EAG region presents intermittent and variable winds that satisfy the Ekman transport and pumping Ekman velocity only for 2 July 2018, which corresponds to the vertical velocity intensification in the EAGF. Although the linear Ekman term in the Ekman pumping velocity (Equation 9) is small or zero ($\nabla_h \times \boldsymbol{\tau}^h \approx 0$), the gradient of the relative vorticity at the surface in the nonlinear Ekman pumping velocity term can drive the Ekman transport and generate vertical velocities (Figure 11; Pallàs-Sanz et al., 2010). Therefore, the Ekman processes play an important role through the westerly down-front winds in the WAGF intensification and vertical velocities development.

The role of the cold filament in the vertical velocities and frontal intensification was shown by studying the filamentogenesis process in the EAGF. The diagnostics for the filamentogenesis snapshot (2 July 2018, 6 hr) show a cold coherent mesoscale filament advecting in the interior of the Mediterranean Sea. Consequently, the evolution of the filamentogenesis was investigated with the horizontal velocities gradient in the frontal tendency equation. The horizontal advection term is predominant in the frontogenesis process and the positive term contribution amplifies the velocities gradient resulting in the EAGF intensification (Dauhajre et al., 2017; Gula et al., 2014). In addition, the horizontal and vertical view of the vertical velocities show a complex pattern. McWilliams

et al. (2009) suggested that filamentogenesis is produced by sharp gradients of buoyancy and velocities, which are identified by an elongated submesoscale filament structure. Additionally, the along front velocity contour is divided in two regions centered on the filament: one flows downstream associated with anticyclonic EAG circulation and the other flows upstream associated with cyclonic circulation in the northeast. The vertical structure of the filamentogenesis, both observed with gliders and simulated by the model, showed pointy density contours in the center of the filament. The deepening of density contours on both sides of the front develops two ASC cells with a sharp downwelling region in the center. However, the ASC cells are not symmetric as in the ideal case of filamentogenesis process. This asymmetry may be an indicator of the frontogenesis arrest described by the filamentogenesis; Gula et al. (2014) reported that the frontal intensification is disrupted by vigorous submesoscale instabilities. Summarizing, the frontogenesis, instabilities processes, and Ekman transport effect do not fully explain the intensification of the EAGF. However, these processes may be responsible for the ASC cells shifting observed in the vertical velocities developed in the EAGF.

In conclusion, during the study period in the Alboran Sea in spring 2018, the spatio-temporal frontal characteristics indicate a wider, deeper and longer-lasting front compared to the EAGF, which are explained by a different frontal dynamics. The frontogenesis mechanism, instabilities processes, and non-linear Ekman effects driven by the AJ and westerly winds, can explain the frontal intensification in the WAGF. As a result, the vertical velocities are developed by a single across-front ASC. Meanwhile, the simulation and observations indicate that the filamentogenesis process may well explain the frontal and vertical velocities development in the EAGF through a cold filament. Additionally, the frontogenesis, instabilities, and Ekman processes play a secondary role in the EAGF, and may be responsible for the asymmetry observed in the ASC cells in the vertical velocities development. Finally, despite the EAGF and WAGF genesis differences, both fronts demonstrate the relevance of submesoscale activity in the intensification of vertical velocities.

The role of the frontogenesis, instabilities, Ekman, and filamentogenesis mechanism in the frontal and vertical velocities intensification in the WAGF and EAGF indicate the significant influence of the submesoscale processes in the frontal dynamics. Furthermore, the conclusions drawn here could be applied to similar locations along the AJ once separated from the influence of the coastal and topographic features; as well to the different periods with similar winds and AJ meandering conditions. The analysis of the forthcoming CALYPSO 2019 field campaign will allow us to further understand the drivers and characteristics of frontal dynamics in the Alboran Sea.

Appendix A: Evaluation of the Glider-Based Observational EPV Calculation

The hypothesis applied to calculate the Ertel potential vorticity (EPV) from a single glider (Equation 5) requires the glider to be piloted perpendicular to the orientation of the front. The calculation of the observational EPV (EPV_{obs}) assumes weak along-front gradients and neglects horizontal gradients of the vertical velocity. To evaluate the impact of the angle of the glider trajectory with respect to the front, we compute the full EPV and EPV_{obs} from daily averaged outputs of the WMOP model and different angles. Three cases for the glider trajectory orientation with respect the EAGF (counterclockwise angle θ) were considered: (a) $\theta = 90°$, (b) $\theta = 45°$, and (c) θ corresponding to the sp56 glider section on 2 July 2018. The comparison of the full EPV and EPV_{obs} calculated for each of the three sections is presented in Figure A1. In the three situations the EPV_{obs} and full EPV show similar spatial variability in the vertical section, yet with a smaller amplitude of EPV_{obs} with respect to the full EPV. Moreover, the EPV_{obs} and full EPV present a similar sign change region in the surface upstream the cross-front section, but the EPV_{obs} shows an additional sign change region downstream that is generated by the underestimation of EPV magnitude. The first row (Figures A1a and A1b) corresponds to $\theta = 90°$, angle for which the EPV_{obs} and full EPV should be identical for an idealized front scenario (with zero along-front velocities variations). For 90° angle, the EPV_{obs} underestimates the magnitude of the full EPV in the frontal region by about 53%. This underestimation comes from the existence of an along-front variability which is not considered in the ideal case. The second row (Figures A1c and A1d) corresponds to $\theta = 45°$, which is an angle likely to lead to larger uncertainties. The impact of the 45° angle on the spatial structure of the observational and full EPV generates an elongated pattern because the front is crossed over a longer distance. For this oblique angle the EPV_{obs} underestimates the magnitude of the full EPV in the frontal region by about 28%. The better estimation obtained with the 45° angle can be explained by the better representation of the across-front velocity variability in the EPV_{obs}. Finally, the third row (Figures A1e and A1f), corresponds to the angle of the glider section sp56 with respect to the front on 2 July 2018 (this angle is estimated to be $\theta = 82°$). The glider section shows similar

results to $\theta = 90°$, but the magnitude underestimation of the full EPV is about 46%. These results indicate that the influence of the angle on the EPV_{obs} computation produces an elongation of the patterns of the EPV, but does not produce any sign change of the EPV in the frontal region. Additionally, the findings indicate that EPV estimates from glider sections crossing the front with an angle different from the ideal $\theta = 90°$ angle are appropriate within the uncertainties associated with the presence of the along-front variability. The underestimation observed in the EPV_{obs} in the three cases can be explained by the presence of (a) a local Rossby number ~ 1 in the frontal region and, (b) significant along-front variations of the velocities, which indicate the importance of ageostrophy. Similar results were reported by Todd et al. (2016), who showed that the angle term in the observational EPV equation had a small contribution, and Viglione et al. (2018), who found that the amplitude of the EPV_{obs} is smaller than the full EPV in the mixed layer. Meanwhile, the underestimation of the EPV_{obs} could be explained by the uncertainty in the along-front velocities variations due to the relative vorticity variance underestimation of the one-ship method (Shcherbina et al., 2013). In conclusion, even if EPV_{obs} underestimates the full EPV, these results justify to analyze the spatial variability of EPV estimates from cross-front observations, even if not strictly perpendicular to the front. In particular, the changes of sign related to conditions for instabilities are expected to be consistent between the observational and full EPV estimates.

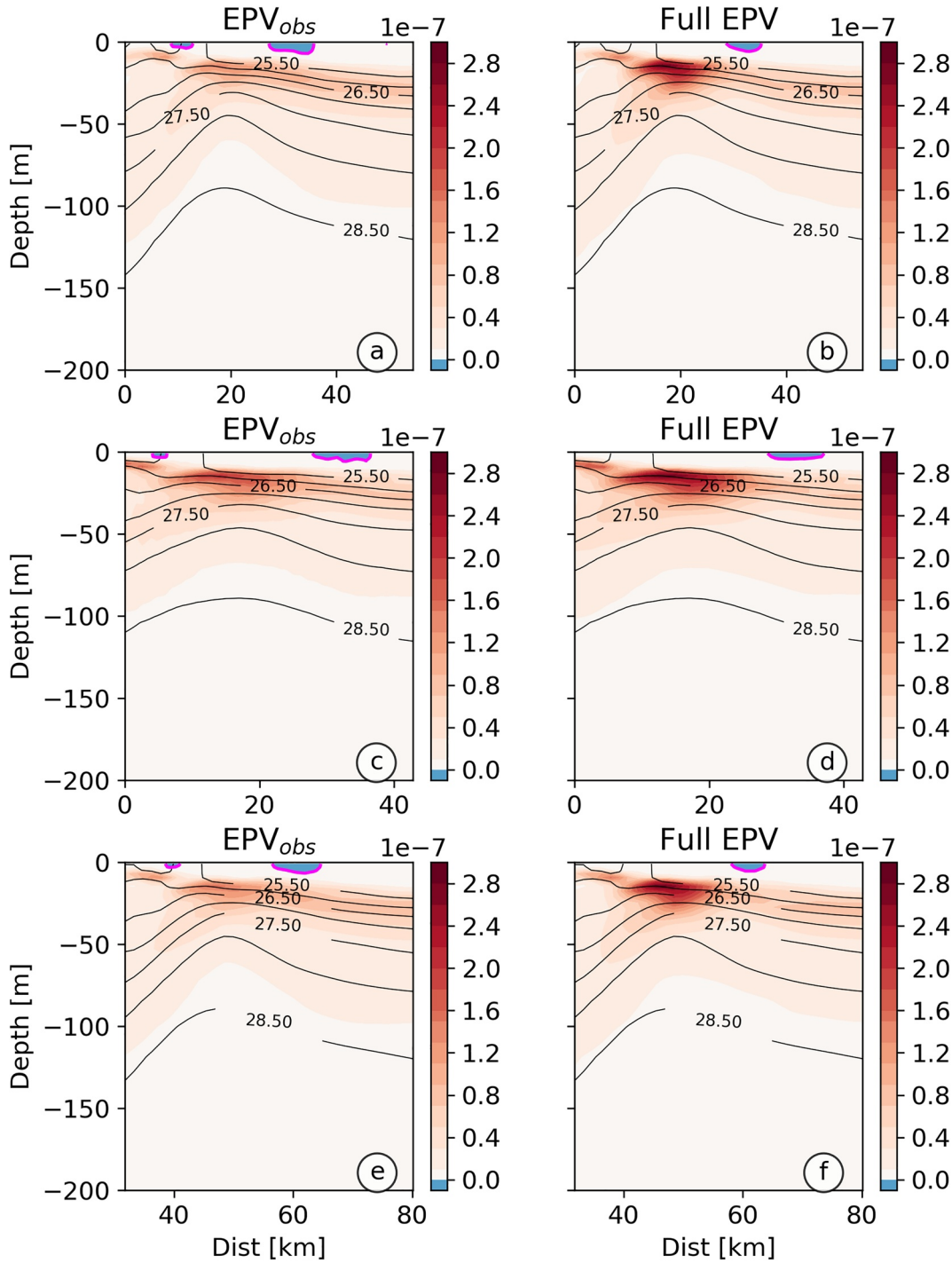

Figure A1. Vertical profile of observational and full Ertel potential vorticity (EPV) from daily averaged outputs of Western Mediterranean OPerational system model (2 July 2018) calculated through three trajectory orientations to the Eastern Alboran Gyre Front (counterclockwise angle θ): (i) $\theta = 90°$ (first row), (ii) $\theta = 45°$ (second row), and (iii) sp56 glider section (third row). The potential density anomaly is indicated by black lines (contour interval is 0.5 kg m^{-3}). The magenta contours show the zero contour of EPV.

Data Availability Statement

The WMOP model is developed by the authors in the Modelling and Forecasting Facility of SOCIB. The model simulation used in this study is available at http://repository.socib.es/repository/entry/show?entryid=b55d389f-87dc-4d9e-ba66-e40cd24c2f2c. The authors are graceful of AEMET and CMEMS for sharing their atmospheric and oceanic model outputs. The CALYPSO observations are available in Rudnick (2021) and Zarokanellos et al. (2021) for glider data and in Dever et al. (2019) for Shipboard UCTD casts data. The chlorophyll-a concentration data is obtained from the MODIS sensor of the Aqua satellite mission developed by GFSC (NASA) and ONR and the sea surface temperature data is a VIIRS/NPP from the NAVO (http://oceancolor.gsfc.nasa.gov/).

Acknowledgments
The authors would like to thank John Allen, as well as ONR CALYPSO colleagues for their helpful suggestions and discussions. This research was supported by SOCIB and CALYPSO project (WHOI Project 13313001—subward A101385) funded by the Office of Naval Research (ONR) Departmental Research Initiatives (M. Garcia-Jove, B. Mourre, N. Zarokanellos, and J. Tintoré). The authors are grateful to the Office of Naval Research (ONR) for research support under grants N00014-18-1-2781 (DRI-CALYPSO) to the Massachusetts Institute of Technology (P. F. J. Lermusiaux) and N00014-18-1-2406 to Scripps Institution of Oceanography (D. L. Rudnick). We acknowledge the technical and scientific staff involved in making measurements during the 2018 ONR Calypso cruise. English revisions by L. Flores Mateos are greatly acknowledged. The authors would also like to thank two anonymous reviewers for their helpful and constructive comments.

References

Adams, K. A., Hosegood, P., Taylor, J. R., Sallée, J. B., Bachman, S., Torres, R., & Stamper, M. (2017). Frontal circulation and submesoscale variability during the formation of a southern ocean mesoscale eddy. *Journal of Physical Oceanography*, *47*(7), 1737–1753. https://doi.org/10.1175/JPO-D-16-0266.1

Allen, J. T., Smeed, D. A., Nurser, A. J., Zhang, J. W., & Rixen, M. (2001). Diagnosis of vertical velocities with the QG omega equation: An examination of the errors due to sampling strategy. *Deep-Sea Research Part I Oceanographic Research Papers*, *48*(2), 315–346. https://doi.org/10.1016/S0967-0637(00)00035-2

Bachman, S. D., Fox-Kemper, B., Taylor, J. R., & Thomas, L. N. (2017). Parameterization of frontal symmetric instabilities. I: Theory for resolved fronts. *Ocean Modelling*, *109*, 72–95. https://doi.org/10.1016/j.ocemod.2016.12.003

Boccaletti, G., Ferrari, R., & Fox-Kemper, B. (2007). Mixed layer instabilities and restratification. *Journal of Physical Oceanography*, *37*(9), 2228–2250. https://doi.org/10.1175/JPO3101.1

Capet, X., McWilliams, J. C., Molemaker, M. J., & Shchepetkin, A. F. (2008). Mesoscale to submesoscale transition in the California current system. Part II: Frontal processes. *Journal of Physical Oceanography*, *38*(1), 44–64. https://doi.org/10.1175/2007jpo3672.1

Capó, E., McWilliams, J. C., Mason, E., & Orfila, A. (2021). Intermittent frontogenesis in the Alboran Sea. *Journal of Physical Oceanography*, *51*(5), 1417–1439. https://doi.org/10.1175/JPO-D-20-0277.1

Dauhajre, D. P., McWilliams, J. C., & Uchiyama, Y. (2017). Submesoscale coherent structures on the continental shelf. *Journal of Physical Oceanography*, *47*(12), 2949–2976. https://doi.org/10.1175/jpo-d-16-0270.1

Dever, M., Freilich, M., Hodges, B. A., Farrar, J. T., Lanagan, T., & Mahadevan, A. (2019). *UCTD and EcoCTD observations from the CALYPSO pilot experiment (2018): Cruise and data report* (Tech. Rep.). Physical Oceanography (PO) WHOI. https://doi.org/10.1575/1912/23637

Dong, J., Fox-Kemper, B., Zhu, J., & Dong, C. (2021). Application of symmetric instability parameterization in the coastal and regional ocean community model (CROCO). *Journal of Advances in Modeling Earth Systems*, *13*(3), e2020MS002302. https://doi.org/10.1029/2020MS002302

du Plessis, M., Swart, S., Ansorge, I. J., & Mahadevan, A. (2017). Submesoscale processes promote seasonal restratification in the subantarctic ocean. *Journal of Geophysical Research: Oceans*, *122*(4), 2960–2975. https://doi.org/10.1002/2016JC012494

Fox-Kemper, B., Ferrari, R., & Hallberg, R. (2008). Parameterization of mixed layer eddies. Part I: Theory and diagnosis. *Journal of Physical Oceanography*, *38*(6), 1145–1165. https://doi.org/10.1175/2007JPO3792.1

Gula, J., Molemaker, M. J., & McWilliams, J. C. (2014). Submesoscale cold filaments in the Gulf Stream. *Journal of Physical Oceanography*, *44*(10), 2617–2643. https://doi.org/10.1175/jpo-d-14-0029.1

Haine, T. W., & Marshall, J. (1998). Gravitational, symmetric, and baroclinic instability of the ocean mixed layer. *Journal of Physical Oceanography*, *28*(4), 634–658. https://doi.org/10.1175/1520-0485(1998)028<0634:GSABIO>2.0.CO;2

Hernandez-Lasheras, J., & Mourre, B. (2018). Dense CTD survey versus glider fleet sampling: Comparing data assimilation performance in a regional ocean model west of Sardinia. *Ocean Science*, *14*(5), 1069–1084. https://doi.org/10.5194/os-14-1069-2018

Hoskins, B. J. (1974). *The role of potential vorticity in symmetric stability and instability* (Vol. 100, No. 425). John Wiley & Sons, Ltd. https://doi.org/10.1002/qj.49710042520

Hoskins, B. J. (1982). The mathematical theory of frontogenesis. *Annual Review of Fluid Mechanics*, *14*(1), 131–151. https://doi.org/10.1146/annurev.fl.14.010182.001023

Hoskins, B. J., & Bretherton, F. P. (1972). Atmospheric frontogenesis models: Mathematical formulation and solution. *Journal of the Atmospheric Sciences*, *29*(1), 11–37. https://doi.org/10.1175/1520-0469(1972)029<0011:afmmfa>2.0.co;2

Jing, Z., Fox-Kemper, B., Cao, H., Zheng, R., & Du, Y. (2021). Submesoscale fronts and their dynamical processes associated with symmetric instability in the northwest pacific subtropical ocean. *Journal of Physical Oceanography*, *51*(1), 83–100. https://doi.org/10.1175/JPO-D-20-0076.1

Juza, M., Mourre, B., Renault, L., Gómara, S., Sebastián, K., Lora, S., et al. (2016). SOCIB operational ocean forecasting system and multi-platform validation in the western mediterranean sea. *Journal of Operational Oceanography*, *9*(sup1), s155–s166. https://doi.org/10.1080/1755876X.2015.1117764

Klein, P., & Lapeyre, G. (2009). The oceanic vertical pump induced by mesoscale and submesoscale turbulence. *Annual Reviews*, *1*(1), 351–375. https://doi.org/10.1146/annurev.marine.010908.163704

Lapeyre, G., & Klein, P. (2006). Dynamics of the upper oceanic layers in terms of surface quasigeostrophy theory. *Journal of Physical Oceanography*, *36*(2), 165–176. https://doi.org/10.1175/JPO2840.1

Large, W. G., & Pond, S. (1981). Open ocean momentum flux measurements in moderate to strong winds. *Journal of Physical Oceanography*, *11*(3), 324–336. https://doi.org/10.1175/1520-0485(1981)011<0324:oomfmi>2.0.co;2

Macías, D., Bruno, M., Echevarría, F., Vázquez, A., & García, C. M. (2008). Meteorologically-induced mesoscale variability of the North-western Alboran Sea (southern Spain) and related biological patterns. *Estuarine, Coastal and Shelf Science*, *78*(2), 250–266. https://doi.org/10.1016/j.ecss.2007.12.008

Mahadevan, A. (2016). The impact of submesoscale physics on primary productivity of plankton. *Annual Review of Marine Science*, *8*(1), 161–184. https://doi.org/10.1146/annurev-marine-010814-015912

Mahadevan, A., Pascual, A., Rudnick, D. L., Ruiz, S., Tintoré, J., & D'Asaro, E. (2021). Coherent pathways for vertical transport from the surface ocean to interior. *Bulletin of the American Meteorological Society*, *101*(11), E1996–E2004. https://doi.org/10.1175/BAMS-D-19-0305.1

Mahadevan, A., & Tandon, A. (2006). An analysis of mechanisms for submesoscale vertical motion at ocean fronts. *Ocean Modelling*, *14*(3–4), 241–256. https://doi.org/10.1016/j.ocemod.2006.05.006

Mahadevan, A., Thomas, L. N., & Tandon, A. (2008). Comment on Eddy/wind interactions stimulate extraordinary mid-ocean plankton blooms. *Science*, *320*(5875), 448b–448. https://doi.org/10.1126/science.1152111

McWilliams, J. C. (2016). Submesoscale currents in the ocean. *Proceedings of the Royal Society A: Mathematical, Physical & Engineering Sciences*, *472*(2189), 20160117. https://doi.org/10.1098/rspa.2016.0117

McWilliams, J. C., Colas, F., & Molemaker, M. J. (2009). Cold filamentary intensification and oceanic surface convergence lines. *Geophysical Research Letters*, *36*(18). https://doi.org/10.1029/2009gl039402

McWilliams, J. C., Gula, J., Molemaker, M. J., Renault, L., & Shchepetkin, A. F. (2015). Filament frontogenesis by boundary layer turbulence. *Journal of Physical Oceanography*, *45*(8), 1988–2005. https://doi.org/10.1175/jpo-d-14-0211.1

McWilliams, J. C., Molemaker, M. J., & Yavneh, I. (2004). Ageostrophic, anticyclonic instability of a geostrophic, barotropic boundary current. *Physics of Fluids*, *16*(10), 3720–3725. https://doi.org/10.1063/1.1785132

Molemaker, M. J., McWilliams, J. C., & Yavneh, I. (2005). Baroclinic instability and loss of balance. *Journal of Physical Oceanography*, *35*(9), 1505–1517. https://doi.org/10.1175/JPO2770.1

Mourre, B., Aguiar, E., Juza, M., Hernandez-Lasheras, J., Reyes, E., Heslop, E., et al. (2018). Assessment of high-resolution regional ocean prediction systems using multi-platform observations: Illustrations in the western Mediterranean Sea. *New Frontiers in Operational Oceanography*, 663–694. GODAE OceanView. https://doi.org/10.17125/gov2018.ch24

Oguz, T., Mourre, B., & Tintoré, J. (2016). Upstream control of the frontal jet regulating plankton production in the Alboran Sea (Western Mediterranean). *Journal of Geophysical Research: Oceans*, *121*(9), 7159–7175. https://doi.org/10.1002/2016JC011667

Oguz, T., Mourre, B., & Tintoré, J. (2017). Modulation of frontogenetic plankton production along a meandering jet by zonal wind forcing: An application to the Alboran Sea. *Journal of Geophysical Research: Oceans*, *122*(8), 6594–6610. https://doi.org/10.1002/2017JC012866

Pallàs-Sanz, E., Johnston, T. M. S., & Rudnick, D. L. (2010). Frontal dynamics in a California current system shallow front: 1. Frontal processes and tracer structure. *Journal of Geophysical Research*, *115*(C12). https://doi.org/10.1029/2009jc006032

Pascual, A., Ruiz, S., Olita, A., Troupin, C., Claret, M., Casas, B., et al. (2017). A multiplatform experiment to unravel meso- and submesoscale processes in an intense front (AlborEx). *Frontiers in Marine Science*, *4*, 39. https://doi.org/10.3389/fmars.2017.00039

Renault, L., Oguz, T., Pascual, A., Vizoso, G., & Tintore, J. (2012). Surface circulation in the Alborn Sea (western Mediterranean) inferred from remotely sensed data. *Journal of Geophysical Research*, *117*(8). https://doi.org/10.1029/2011JC007659

Robinson, A. R., Sellschopp, J., Warn-Varnas, A., Leslie, W. G., Lozano, C. J., Haley, P. J., et al. (1999). The Atlantic Ionian stream. *Journal of Marine Systems*, *20*(1–4), 129–156. https://doi.org/10.1016/S0924-7963(98)00079-7

Rudnick, D. L. (2021). *Observations of the Almeria-Oran front in the Mediterranean Sea using spray underwater gliders* (Data set). https://doi.org/10.21238/S8SPRAY3700

Rudnick, D. L., & Klinke, J. (2007). The underway conductivity-temperature-depth instrument. *Journal of Atmospheric and Oceanic Technology*, *24*(11), 1910–1923. https://doi.org/10.1175/JTECH2100.1

Ruiz, S., Claret, M., Pascual, A., Olita, A., Troupin, C., Capet, A., et al. (2019). Effects of oceanic mesoscale and submesoscale frontal processes on the vertical transport of phytoplankton. *Journal of Geophysical Research: Oceans*, *124*(8), 5999–6014. https://doi.org/10.1029/2019JC015034

Rypina, I. I., Getscher, T. R., Pratt, L. J., & Mourre, B. (2021). Observing and quantifying ocean flow properties using drifters with drogues at different depths. *Journal of Physical Oceanography*, *51*(8), 2463–2482. https://doi.org/10.1175/jpo-d-20-0291.1

Sasaki, H., Klein, P., Qiu, B., & Sasai, Y. (2014). Impact of oceanic-scale interactions on the seasonal modulation of ocean dynamics by the atmosphere. *Nature Communications*, *5*. https://doi.org/10.1038/ncomms6636

Shchepetkin, A. F., & McWilliams, J. C. (2005). The regional oceanic modeling system (ROMS): A split-explicit, free-surface, topography-following-coordinate oceanic model. *Ocean Modelling*, *9*(4), 347–404. https://doi.org/10.1016/j.ocemod.2004.08.002

Shcherbina, A. Y., D'Asaro, E. A., Lee, C. M., Klymak, J. M., Molemaker, M. J., & McWilliams, J. C. (2013). Statistics of vertical vorticity, divergence, and strain in a developed submesoscale turbulence field. *Geophysical Research Letters*, *40*(17), 4706–4711. https://doi.org/10.1002/grl.50919

Smith, W. H. F., & Sandwell, D. T. (1997). Global sea floor topography from satellite altimetry and ship depth soundings. *Science*, *277*(5334), 1956–1962. https://doi.org/10.1126/science.277.5334.1956

Sullivan, P. P., & McWilliams, J. C. (2018). Frontogenesis and frontal arrest of a dense filament in the oceanic surface boundary layer. *Journal of Fluid Mechanics*, *837*, 341–380. https://doi.org/10.1017/jfm.2017.833

Taylor, J. R., & Ferrari, R. (2009). On the equilibration of a symmetrically unstable front via a secondary shear instability. *Journal of Fluid Mechanics*, *622*, 103–113. https://doi.org/10.1017/S0022112008005272

Thomas, L., & Ferrari, R. (2008). Friction, frontogenesis, and the stratification of the surface mixed layer. *Journal of Physical Oceanography*, *38*(11), 2501–2518. https://doi.org/10.1175/2008JPO3797.1

Thomas, L. N. (2005). Destruction of potential vorticity by winds. *Journal of Physical Oceanography*, *35*(12), 2457–2466. https://doi.org/10.1175/jpo2830.1

Thomas, L. N., & Lee, C. M. (2005). Intensification of ocean fronts by down-front winds. *Journal of Physical Oceanography*, *35*(6), 1086–1102. https://doi.org/10.1175/jpo2737.1

Thomas, L. N., Taylor, J. R., D'Asaro, E. A., Lee, C. M., Klymak, J. M., & Shcherbina, A. (2016). Symmetric instability, inertial oscillations, and turbulence at the Gulf Stream front. *Journal of Physical Oceanography*, *46*(1), 197–217. https://doi.org/10.1175/JPO-D-15-0008.1

Thomas, L. N., Taylor, J. R., Ferrari, R., & Joyce, T. M. (2013). Symmetric instability in the Gulf Stream. Deep-sea research Part II. *Topical Studies in Oceanography*, *91*, 96–110. https://doi.org/10.1016/j.dsr2.2013.02.025

Thompson, A. F., Lazar, A., Buckingham, C., Garabato, A. C., Damerell, G. M., & Heywood, K. J. (2016). Open-ocean submesoscale motions: A full seasonal cycle of mixed layer instabilities from gliders. *Journal of Physical Oceanography*, *46*(4), 1285–1307. https://doi.org/10.1175/JPO-D-15-0170.1

Tintoré, J., Gomis, D., Alonso, S., & Parrilla, G. (1991). Mesoscale dynamics and vertical motion in the Alborán Sea. *Journal of Physical Oceanography*, *21*(6), 811–823. https://doi.org/10.1175/1520-0485(1991)021<0811:mdavmi>2.0.co;2

Tintoré, J., Vizoso, G., Casas, B., Heslop, E., Pascual, A., Orfila, A., et al. (2013). SOCIB: The Balearic Islands coastal ocean observing and forecasting system responding to science, technology and society needs. *Marine Technology Society Journal*, *47*(1), 101–117. https://doi.org/10.4031/MTSJ.47.1.10

Todd, R. E., Owens, W. B., & Rudnick, D. L. (2016). Potential vorticity structure in the North Atlantic western boundary current from underwater glider observations. *Journal of Physical Oceanography*, *46*(1), 327–348. https://doi.org/10.1175/JPO-D-15-0112.1

Vélez-Belchí, P., & Tintoré, J. (2001). Vertical velocities at an ocean front. *Scientia Marina*, *65*(S1), 291–300. https://doi.org/10.3989/scimar.2001.65s1291

Viglione, G. A., Thompson, A. F., Flexas, M. M., Sprintall, J., & Swart, S. (2018). Abrupt transitions in submesoscale structure in Southern Drake Passage: Glider observations and model results. *Journal of Physical Oceanography*, *48*(9), 2011–2027. https://doi.org/10.1175/JPO-D-17-0192.1

von Appen, W. J., Wekerle, C., Hehemann, L., Schourup-Kristensen, V., Konrad, C., & Iversen, M. H. (2018). Observations of a submesoscale cyclonic filament in the marginal ice zone. *Geophysical Research Letters*, *45*(12), 6141–6149. https://doi.org/10.1029/2018GL077897

Zarokanellos, N. D., Rudnick, D. L., Garcia-Jove, M., Mourre, B., Ruiz, S., Pascual, A., & Tintoré, J. (2022). Frontal dynamics in the Alboran Sea: 1. Coherent 3D pathways at the Almeria-Oran front using underwater glider observations. *Journal of Geophysical Research: Oceans*. https://doi.org/10.1029/2021JC017405

Zarokanellos, N. D., Rudnick, D. L., & Tintoré, J. (2021). *SOCIB CALYPSO glider observations (version 1.0.0)* (Data set). Balearic Islands Coastal Observing and Forecasting System, SOCIB. https://doi.org/10.25704/QMZF-VV36